International Journal of Heat and Mass Transfer 128 (2019) 649–667

Contents lists available at ScienceDirect

International Journal of Heat and Mass Transfer

journal homepage: www.elsevier.com/locate/ijhmt

Two-phase frictional pressure drop in a thin mixed-wettability microchannel

James M. Lewis, Yun Wang *

Renewable Energy Resources Laboratory, National Fuel Cell Research Center, and Department of Mechanical and Aerospace Engineering, University of California, Irvine 92697-3975, CA, United States

ARTICLE INFO

Article history:
Received 30 May 2018
Received in revised form 1 August 2018
Accepted 2 September 2018
Available online 15 September 2018

Keywords:
Two-phase flow
Air-water
Frictional pressure drop
Mixed-wettability
Microchannel

ABSTRACT

This study focuses on the experimental investigation of the two-phase pressure drop in a thin mixed-wettability microchannel. Air-water flows in a thin microchannel of dimensions 3.23 mm wide by 0.304 mm high. The test conditions primarily produce rivulet flow. The two-phase pressure drop increases when the base contact angle changes from 76° to 99°, with the other walls remaining the same. Combining the result with existing literature demonstrates that consistent behavior in the change of the two-phase pressure when comparing different wettabilities arises with careful consideration of the experimental parameters to classify experiments of adiabatic two-phase flow in a single microchannel into three categories: homogeneous, hydrophobic mixed-wettability, and superhydrophobic mixed-wettability microchannels. The two-phase pressure measurements also allow for the assessment of homogeneous, separated, and relative permeability models. Limiting the analysis to the rivulet flow regime allows for the determination of a new relative permeability exponent of 1.747 in the two-fluid model, which produces a mean absolute percent error of 14.9%. However, the models do not fully collapse the data, indicating differing air-water interactions. The work discusses possible causes of this behavior from experimental limitations to instabilities of the rivulet flow.

1. Introduction

Surface characteristics of microchannels can impact the performance of various devices. For example in thermal management devices, hydrophobicity impacts flow transition and heat transfer rate for condensing flow in microchannels [1]. Similarly, hydrophobic surfaces influence the heat transfer characteristics of flow boiling in microchannels [2,3]. The change in hydrophobicity leads to a change in the pressure drop of the channel, in which a significant increase could render the design impractical for its intended application. Polymer-electrolyte membrane (PEM) fuel cells represent another application that relies on differing surface wettabilities to manage water generated by the hydrogen-oxygen reaction. In PEM fuel cells, a gas-diffusion layer (GDL) forms one side of cathode gas supply channels, with the remaining three sides formed by the bipolar plate. To prevent water retention, commercial GDLs undergo a hydrophobic treatment [cf. 4,5]. The bipolar plate can have a different wettability than the GDL [cf. 6–8], resulting in a mixed-wettability microchannel. Understanding the two-phase flow behavior and corresponding pressure drop can aid in designing a successful water management strategy for optimal performance.

Research focuses on understanding the impact of surface wettability on the behavior of the flow and the corresponding two-phase pressure. Unfortunately, studies of the two-phase pressure drop as a function of channel wettability have produced inconsistent results in how the two-phase pressure drop changes when comparing similar microchannels with different wettability (Section 2.1). Furthermore, the prediction of the two-phase pressure drop in hydrophobic microchannels usually relies on models experimentally determined for flows in hydrophilic microchannels. Some alternatives exist such as the separated flow models of Lee & Lee [9] and Wang et al. [10] but require assessment in their applicability to other flows. Therefore, improvements in predicting the two-phase pressure in hydrophobic channels relies on the continual assessment of existing models and an understanding of how the flow characteristics influence the accuracy of the prediction.

Through an experimental study in a mixed-wettability microchannel compared to a previous study in an identical hydrophilic microchannel [11] this work seeks to: (1) determine how the flow behavior changes between the two cases, (2) address the differences in existing literature for the two-phase pressure trend with contact angle to provide guidelines for future work, and (3)

---

* Corresponding author.
E-mail address: yunw@uci.edu (Y. Wang).

https://doi.org/10.1016/j.ijheatmasstransfer.2018.09.010
0017-9310/Published by Elsevier Ltd.

assess the predictive accuracy of existing two-phase pressure drop models including determining new relative permeability exponents (n_k) in the two-fluid model for the flow patterns observed in this work. Section 2 details the conflicting results for the two-phase pressure drop presented in literature (Section 2.1) and a discussion of the stability of rivulets (Section 2.2), the primary flow pattern observed in this study. A discussion of the methods used to predict the two-phase pressure follows in Section 3. Section 4 details the experimental method to produce air-water flow in a mixed-wettability microchannel of dimensions 3.23 mm wide by 0.304 mm high by 164 mm long. The subsequent section presents the validation of the experimental set-up (Section 5.1), the two-phase pressure drop results (Section 5.2), and the observed flow patterns (Section 5.3). Section 5.4 discusses classifying the results of existing literature and the current work to provide consistent trends for the two-phase pressure change with contact angle. The comparison to the existing two-phase pressure models follows in Section 5.5 with the determination of an optimized relative permeability exponent (n_k) for rivulet flow (Section 5.6). The work concludes with a discussion of experimental limitations and rivulet stability that can influence the predictive ability of the assessed two-phase pressure models (Section 5.7).

2. Background

2.1. Two-phase pressure and flow pattern

Investigations of two-phase flow in microchannels consisting of at least one hydrophobic surface have produced inconsistent findings in terms how the two-phase pressure drop changes when comparing the hydrophobic to hydrophilic experiments. A mixed-wettability rectangular microchannel has at least one wall of a distinctly different wettability than the other three. The contact angle (θ) defines the surface wettability (Table 1). Specifically, surface wettability falls into two categories: hydrophilic when $\theta < 90^\circ$ and hydrophobic when $\theta > 90^\circ$.

Stevens et al. [12] conducted air-water experiments in a microchannel 9.92 mm wide by 360–380 μm high. The microchannel consisted of three hydrophilic acrylic surfaces with a contact angle of 64° and one interchangeable surface. The interchangeable surface consisted of a hydrophilic silicon surface of $\theta = 60^\circ$ for the control tests and a superhydrophobic surface for the remaining tests. The superhydrophobic surface consisted of parallel ribs 15–20 μm in height with differing cavity ratios (ratio of rib surface area divided by the total plate surface area). The superhydrophobic surface had contact angles of 146°, 157°, & 155° in the streamwise direction and 132°, 149°, & 146° in the transverse direction, depending on the cavity fraction. The pressure measurements by Stevens et al. [12] showed little influence of the cavity fractions on the two-phase flow multiplier (ϕ) but saw a reduction of 10% in ϕ—beyond the 5–15% reduction in the single-phase measurement—relative to the prediction of Kim & Mudawar [13]. The control experiments agreed within a mean absolute percent error within 20% of the prediction of Kim & Mudawar [13]. The gas Reynolds number (Re_G) varied between 22 and 215 and the liquid Reynolds number (Re_L) varied between 55 and 220, which generated slug flow.

Table 1
Definition of wettability.

Contact angle [°]	Wettability
0	Wetting
$0 < \theta < 90$	Partially wetting
$90 \leqslant \theta < 180$	Partially non-wetting
180	Non-wetting

Wang et al. [14] also studied the influence of superhydrophobic surfaces on the two-phase pressure, finding inconsistent results. The microchannel had a 4 mm square cross-section with a 150 mm length consisting of a plexiglass top with the remaining walls formed by graphite with different surface treatments. It remains unclear as to the contact angle of the plexiglass, although typically plexiglass behaves hydrophilicly. The surface treatment of the graphite produced a contact angle of 35° with silica particles, 145° when treated with PTFE, or 155° when treated with silica combined with PDMS-2. At a superficial liquid velocity (U_L) of 0.015 m/s with superficial gas velocities (U_G) between 2 and 9 m/s, the PTFE treatment resulted in a higher two-phase pressure drop than the silica treatment. The silica-PDMS-2 treatment resulted in the lowest two-phase pressure drop of the three configurations.

Cho & Wang [15] investigated two-phase air–water flow in a microchannel of dimensions $1.68 \times 1.00 \times 150$ mm^3 with $0.55 \leqslant U_G \leqslant 9.36$ m/s and $5.0 \times 10^{-5} \leqslant U_L \leqslant 1.0 \times 10^{-3}$ m/s. The hydrophilic surface had a contact angle of 80° and the smooth hydrophobic PTFE surface had a contact angle of 104°. Identical hydrophilic surfaces formed the remainder of the microchannel in both cases. Contrary to Stevens et al. [12] and Wang et al. [14], the two-phase pressure drop increased with the increased base contact angle. A comparison to existing two-phase pressure models showed good agreement between the prediction and the experimental data, with increasing agreement as U_L increased. When optimizing the relative permeability exponent (n_k), Cho & Wang [15] found a slight increase from 1.96, 2.15, & 2.49 in the hydrophilic case to 2.47, 2.58, and 2.89 in the hydrophobic case for annular, mixed flow, & slug flow, respectively. In both the hydrophilic and hydrophobic cases, similar flow patterns existed, with a slight redistribution of fluid to the hydrophilic corners in the hydrophobic case. A rough carbon paper with a contact angle 128° also showed a pressure increase but existing two-phase pressure models did not compare well to the experimental data.

Lu et al. [8] investigated the influence of surface wettability in 8 parallel rectangular channels, 0.4 mm deep by 0.7 mm wide. Water injection occurred through a gas-diffusion layer (GDL) with a contact angle of 138–145°. Different surface treatments on the remaining three walls produced contact angles of 11°, 85°, and 116°. At $U_L = 3.0 \times 10^{-4}$ m/s, the two-phase pressure increased with the contact angle in a range of superficial gas velocities between 0.98 m/s and 15 m/s but became similar for U_G between 15 and 29.5 m/s. Conversely, at $U_L = 7.5 \times 10^{-4}$ m/s, the two-phase pressure generally decreased as the contact angle increased between $U_G = 0.98$–29.5 m/s. The authors noted the hydrophilic channel meets the Concus-Finn condition for water to wick into the corners. As a result, the water moved in the channel as a continuous film instead of being sheared by the air flow, which caused the slightly higher two-phase pressure.

Unlike the four previous works in which the authors conducted experiments under adiabatic conditions, Phan et al. [16] conducted flow boiling experiments with different surface wettabilities. Different surface treatments resulted in contact angles of 26°, 49°, 63°, and 103° for three of the walls, with a hydrophilic Pyrex glass top. The microchannel had dimensions 0.5 mm high by 5 mm wide by 180 mm long. Under total mass fluxes of water between 100 and 120 kg/m^2 s, the two-phase pressure increased with increasing contact angle but existing two-phase pressure models did not well predict the behavior.

The five aforementioned works studied mixed-wettability channels, in which at least one surface had a differing wettability than the remaining three. Several authors have studied homogeneous rectangular channels, where all four walls have the same wetting properties. Wang et al. [10] studied 200 μm wide by 100 μm deep microchannels of glass, modified glass, and PDMS that had contact angles of 37°, 94°, and 135°, respectively. Testing at $U_L = 0.08$ and 0.12 m/s produced slug flow for $U_G = 0.05$–0.4 m/s. The test conditions of $U_L = 0.05$ and 0.18 m/s for $U_G = 1.0$–4.0 m/s produced continuous gas flows—the gas forms a continuous path from one end of the channel to the other. In both cases, the two-phase pressure decreased as the contact angle increased.

Choi et al. [17] also studied homogeneous microchannels with different contact angles for nitrogen-water flows at $0.066 \leqslant U_G \leqslant 34.1$ m/s and $0.19 \leqslant U_L \leqslant 0.46$ m/s. The rectangular microchannels had cross-sections of 608.6 μm wide by 410 μm high for the hydrophilic channel and 617.2 μm wide by 430.6 μm for the hydrophobic channel. Bare photosensitive glass with a contact angle of 25° formed the hydrophilic microchannel while a treated photosensitive glass with a contact angle of 105° formed the hydrophobic microchannel. While the hydrophilic case produced bubbly and liquid-ring flows, the hydrophobic case produced stratified flow with and without the entrainment of nitrogen. Consequently, the two-phase pressure decreased as the contact angle increased. Using existing correlations of the Chisholm parameter (C), the authors could not predict the two-phase pressure in the hydrophobic case.

Finally, Rapolu & Son [18] investigated the influence of contact angle on air-water slug flow in square microchannels of dimensions 700 μm². The microchannels had contact angles of 25°, 60°, 105°, and 150°. In the range of liquid volumetric flow rates (Q_L) of 1.2×10^{-8} to 4.6×10^{-8} m³/s and gas volumetric flow rates (Q_G) of 1.4×10^{-6} to 1.7×10^{-6} m³/s, the two-phase pressure increased as the contact angle increased. Combined with the other works discussed, the trend of changing contact angle on the two-phase pressure remains unclear.

By changing the contact angle, the two-phase flow patterns typically change as well. Barajas & Panton [19] studied air–water flow in mini-tubes of 1.6 mm diameter with contact angles of 34°, 61°, 74°, and 106°. The contact angle did not significantly alter the conditions at which slug, bubble, or dispersed flow formed. As the contact angle increased, rivulet flows replaced wavy flows for contact angles above 61° and multiple rivulets replaced annular flow above $\theta = 74°$. Lee & Lee [20] found general agreement with Barajas & Panton [19] but noted that the flow could appear similar but have different interactions with the wall. For example, the authors defined a wet-plug flow in which a thin water film lubricated the gas plugs whereas dry-plug flow does not have the lubricating film and directly contacts the wall. Huh et al. [21] studied air-water flow in microchannels 300 μm wide by 100 μm high. Under a range of gas and liquid superficial velocities, the authors identified 7 distinct flow patterns in the hydrophobic channel with a contact angle of 111°. In contrast, hydrophilic channels of contact angles 35° and 75° produced only two flow patterns; only one flow pattern, the annular-droplet flow, overlapped between the hydrophilic and hydrophobic cases. While the flow can behave similarly, the flow patterns often change with changing contact angle.

2.2. Rivulet stability

Rivulet flows seen by Barajas & Panton[19] and Lee & Lee [20] can become unstable due to perturbations of the flow. When a rivulet becomes unstable, its leading edge breaks apart into periodic droplets, where the wavelength of the instability nearly equals the average drop spacing [22], changing the behavior of the flow. Davis [23] investigated the linear stability of infinite static rivulets on an inclined plane. With fixed contact lines, the rivulet has unconditional stability for all axial wavenumbers (k) if the surface has a contact angle less than $\pi/2$. If the surface contact angle falls in the range $\pi/2 < \theta < \pi$, the rivulet will remain stable for $(kR)^2 > 1$, where R is the radius of curvature of the rivulet. If the contact lines can move but maintain a constant contact angle, a region of stability exits that does not encompass a complete range of wavenumbers (i.e. for a given wavenumber, instabilities will grow for a surface of contact angle $\pi/4$ but become stable for a contact angle of $\pi/2$.

Koplik et al. [24] investigated the linear pearling instability of rivulets confined to a chemical channel, in which a gravitational force drives the liquid rivulet. A chemical channel consists of a wetting surface surrounded by non-wetting surfaces. The authors noted in the static case, instabilities grow for $\theta > \pi/2$. The driving force enhances the instability, if the instability also occurred in the static case. The driving force could not destabilize a stable state that exists in the static case.

Herrada et al. [25] simulated horizontal air-ethanol flow in a microchannel of constant pressure gradient, where rivulets flow along a chemical channel. The surface had contact angles of 80°, 89°, and 120°. The case of $\theta = 80°$ remained stable. However, the 89° and 120° cases demonstrated that the ethanol rivulets surrounded by a gas flow became unstable above a critical Reynolds number. The Weber number shifts the peak growth factor. Both the Reynolds number and Weber number are calculated from the properties of the rivulet and based on an average velocity inside the rivulet. The authors did not note the influence of the air velocity/Reynolds number.

Cheverda et al. [26] conducted experiments of FC-72/nitrogen flows in a $67 \times 30 \times 1.4$ mm³ microchannel specifically designed to generate rivulet flow. Under a wide range of liquid and gas Reynolds numbers the authors showed as the liquid Reynolds number increased for a fixed gas Reynolds number the rivulet width increases. Conversely as the gas Reynolds number increased for a fixed liquid Reynolds number the rivulet width decreases. In either case, the surface becomes wavier (less stable).

3. Two-phase pressure drop models

The prediction of the two-phase pressure drop relies on semi-empirical models that typically fall into three categories: homogeneous, separated, and relative permeability based models. For brevity, this section introduces the different methods but does not repeat the equations defining the individual models, which the reader can find in the previous work [11] and in the cited works.

3.1. Homogeneous flow models

A homogeneous flow model treats the two-phase flow as an equivalent single-phase flow with averaged properties. The two-phase viscosity (μ_{tp}) and the two-phase density (ρ_{tp}) determine the two-phase Reynolds number (Re_{tp}), used to determine the friction factor, such that the two-phase pressure equals:

$$\left(\frac{dP}{dz}\right)_{tp} = f_{tp}\frac{G^2}{2D_H\rho_{tp}} \tag{1}$$

where P stands for pressure, z the downstream coordinate, f the Darcy friction factor, G the total mass flux, D_H the hydraulic diameter, and ρ the density. The subscript tp stands for two-phase. Several models for the two-phase viscosity exist and vary in terms of the weighting factor of either the gas or liquid viscosity [27–33].

3.2. Separated flow model

The separated flow models follow the work of Lockhart & Martinelli [34] and Chisholm [35] to account for the interaction of the phases. Lockhart & Martinelli proposed the two-phase pressure equals:

$$\left(\frac{\Delta P}{\Delta L}\right)_{tp} = \phi_G^2 \left(\frac{\Delta P}{\Delta L}\right)_G \tag{2}$$

for a channel of length L. The subscripts G and L refer to the gas and liquid phase, respectively. The gas two-phase flow multiplier (ϕ_G^2) depends on the Lockhart-Martinelli parameter (X):

$$X = \sqrt{\frac{\Delta P_L}{\Delta P_G}} \tag{3}$$

in which ΔP_L and ΔP_G equal the pressure drop experienced along the channel if the respective phase flowed alone. Chisholm proposed:

$$\phi_G^2 = 1 + CX + X^2 \tag{4}$$

where C, the Chisholm parameter, can take different forms. Chisholm [35] proposed that $C = 5$ for laminar flows of both phases but applying the separated flow model to microchannels required modifying the C-value. For example, the C-value can remain a constant modified by constant test parameters [36–39]. Conversely, the C-value could vary as a function of varying test parameters [40,41,13,42–44].

Two authors proposed C-value correlations specific to hydrophobic channels, which this work assesses. Lee & Lee [9] modified a correlation derived for hydrophilic channels [cf. 43] to account for the moving contact lines that result in dry flows such that:

$$C = 2.161 \times 10^{-21} \Lambda^{-3.703} \Phi^{-0.995} Re_{lo}^{0.486} \tag{5}$$

The test conditions and fluid properties modify C through:

$$\Phi = \frac{\mu_L \overline{U}}{\sigma} \tag{6}$$

$$\Lambda = \frac{\mu_L^2}{D_H \rho_L \sigma} \tag{7}$$

$$Re_{lo} = \frac{GD_H}{\mu_L} \tag{8}$$

The term Φ represents a capillary number based on the sum of the superficial velocities ($\overline{U}$) and depends on the surface tension of the gas-liquid pair (σ). The inverse liquid-only Suratman number (Λ) accounts for the combined influence of inertia and surface tension to the influence of the liquid viscosity. The liquid-only Reynolds number (Re_{lo}) represents the relative importance between the inertia of the total mass flux to the viscous force of the liquid as a function of the dynamic liquid viscosity (μ_L) and the hydraulic diameter (D_H). The total mass flux, G, equals:

$$G = \frac{\rho_G Q_G + \rho_L Q_L}{A_c} \tag{9}$$

which depends on the density (ρ), the volumetric flow rate (Q), and the cross-sectional area of the channel (A_C). Wang et al. [10] proposed:

$$C = 18.1(1 + \cos\theta)^{0.200} We_L^{0.248} \tag{10}$$

which takes into account the influence of the contact angle (θ) and the relative importance between the liquid inertia and surface tension through the liquid Weber number defined as:

$$We_L = \frac{\rho_L U_L^2 D_h}{\sigma} \tag{11}$$

3.3. Relative permeability models

Although typically applied for porous media, Cho & Wang [45] and Lewis & Wang [11] showed the relative permeability models can predict the two-phase pressure in microchannels. Wang [46] derived:

$$\phi_G^2 = \bar{z}^* + \int_{\bar{z}^*}^{1} \frac{1}{k_{r,G}} d\hat{z} \tag{12}$$

where the term $\bar{z}^*$ equals the location of water injection divided by the length of the channel and accounts for the flow initially starting as single-phase gas flow. The gas relative permeability ($k_{r,G}$) can have different forms but generally has the form:

$$k_{r,G} = (1 - s_{L,e})^{n_k} \tag{13}$$

where the value of the relative permeability exponent (n_k) changes depending on the flow pattern. Several authors have proposed relations for $k_{r,G}$ [47–51,31]. The gas relative permeability depends on the effective liquid saturation ($s_{L,e}$) which equals the liquid saturation by neglecting any irreducible liquid saturation ($s_{L,r}$)—water in the channel that the gas stream cannot remove.

Typically, researchers measure the liquid saturation. However, Fourar & Bories [31] proposed a saturation model to accompany the authors' relative permeability model as:

$$s_L = \left(\frac{X}{1+X}\right)^2 \tag{14}$$

Wang [46] arrived at a model for the saturation dependent on the relative permeability exponent (n_k) as:

$$s_L = \frac{\left(\frac{U_L \mu_L}{U_G \mu_G}\right)^{\frac{1}{n_k}} + s_{L,r}}{\left(\frac{U_L \mu_L}{U_G \mu_G}\right)^{\frac{1}{n_k}} + 1} \tag{15}$$

Herein, the two-fluid model refers to Eq. (13) combined with Eqs. (12) and (15).

4. Experimental method

The experimental work consists of air-water tests in a mixed-wettability rectangular microchannel where a hydrophobic surface forms the base and hydrophilic surfaces form the remainder of the channel. A previous investigation [11] provides the hydrophilic results for comparison. To accurately access the influence of changing the base from hydrophilic to hydrophobic, this work replicates the same test conditions as the hydrophilic case. Calculating different terms relies on standard fluid properties of humid air and water at 20 °C shown in Table 2. Water volumetric flow rates of 177 μL/h, 1.77 mL/h, 59.07 μL/min, and 590.7 μL/min produce superficial liquid velocities of $5.0 \times 10^{-5}, 5.0 \times 10^{-4}, 1.0 \times 10^{-3}$, and 1.0×10^{-2} m/s, respectively. The four superficial liquid velocities form four different data sets. For each data set, the gas volumetric flow rates vary from 30 and 50–325 mL/min in 25 mL/min increments producing superficial gas velocities between 0.51 and 5.50 m/s. Characterizing the flow in terms of Reynolds numbers gives a Re_L of 0.0277, 0.277, 0.55, and 5.55 with gas Reynolds numbers varying between 18.2 and 197 for each liquid Reynolds number. The combination of Reynolds numbers produce a liquid-only Reynolds number between 0.35 and 9.19.

Table 2
Fluid properties.

Property	Air	Water
Density (kg/m^3)	1.19	998.3
Viscosity (kg/m s)	1.846×10^{-5}	1.002×10^{-3}
Surface tension (N/m)	72.86×10^{-3}	

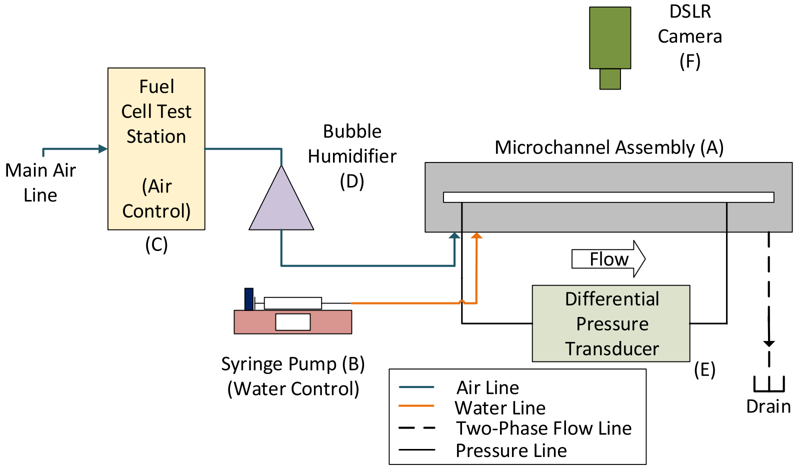

Fig. 1. Schematic diagram of the experimental set-up.

Table 3
Microchannel dimensions.

Height (mm)	Width (mm)	Length (mm)
0.304 ± 0.015	3.23 ± 0.01	164 ± 0.5

4.1. Experimental assembly

The design of the microchannel assembly (Fig. 1A), in which individual layers form the channel, allows for one layer to change while the other layers remain the same. Thus, the mixed-wettability experiments use the same microchannel assembly as the hydrophilic experiments, except the base material changed from aluminum to PTFE. Table 3 shows the microchannel dimensions and the corresponding uncertainty. The change from a 6061 aluminum base to a PTFE base changed the base contact angle from $76^\circ \pm 8^\circ$ to $99^\circ \pm 10^\circ$ for air-water. The 304 full-hard stainless steel forming the side walls and polycarbonate forming the top of the channel have contact angles of $82^\circ \pm 7^\circ$ and $81^\circ \pm 7^\circ$, respectively. In this work, the stated uncertainties are at a 95% confidence level.

The air and water flow enter the channel independently. Single-phase gas flows in the channel for the first 10 mm of the channel length, at which point water injection occurs through a 365 μm hole in the base (Fig. 2a). A New Era Pump System NE-300 syringe pump (Fig. 1B) supplies room temperature (20 °C ±2 °C) deionized water to the system. MKS 100B mass flow controllers inside a Scribner and Associates 850e Fuel-cell Test Station (Fig. 1C) control the air flow from the main air supply within ±20 mL/min. The air passes through a bubble humidifier (Fig. 1D) containing 1500 mL of DI-water to achieve 100% relative humidity before entering the microchannel.

Finally, a Setra 230 differential pressure transducer (Fig. 1E) with a range of ±0.5 psi (±3.447 kPa) provides the differential pressure between two pressure taps with an accuracy of ±0.0025 psi (±17.2 Pascals). The measured pressure difference occurs over a 152 mm length of the channel, with one tap located at the entrance ($z = 0$ mm) and another one located 12 mm before the exit ($z = 152$ mm) as shown in Fig. 2b. To eliminate noise and improve the dynamic range of the voltage signal output from the Setra 230, the signal undergoes signal conditioning. A precision buck and gain amplifier subtracts out the mean voltage before amplifying the signal by a factor of 10. A digital filter (Alligator USBPGF-S1) filters the pressure signal at 700 Hz—selected to put the 3 dB point beyond the 500 Hz frequency response of the pressure transducer—before a data acquisition card (DATAQ DI-245) logs the signal at 2000 samples per second.

4.2. Flow visualization

The clear polycarbonate sheet forming the top of the channel gives optical access for a DSLR camera (Canon Rebel T3, Fig. 1F) to capture images of the entire channel length in 5 s intervals to determine the flow characteristics. The length of the channel compared to the channel width make it difficult to demonstrate the behavior of the flow for the multiple test conditions. Therefore, this work presents the flow behavior in two forms. The first form consists of traces of the flow with a compressed aspect ratio, allowing for a clear comparison between different experiments. The second presents real images of the primary flow structures in a section of

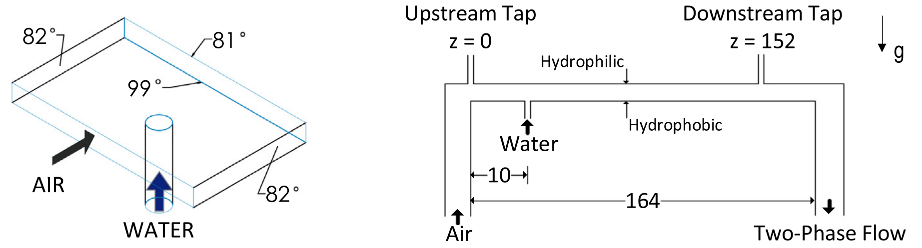

(a) Diagram of asymmetric water injection and the wettability of the channel walls.

(b) Pressure tap locations. Dimensions are in millimeters.

Fig. 2. Detailed diagram of the microchannel assembly.

the channel, where the image maintains the true aspect ratio but with modified image properties (contrast, saturation, sharpness, and smoothness) to improve the clarity of the flow structures.

5. Results and discussion

5.1. Single-phase validation

Single-phase experiments of gas flow validate the experimental apparatus through a comparison to the theoretical result and single-phase measurements for the hydrophilic case. For single-phase flow in a rectangular duct, the Darcy friction factor (f) depends on the aspect ratio of the channel as:

$$\overline{C} = 96(1 - 1.35532\alpha^{*} + 1.9467\alpha^{*2} - 1.7012\alpha^{*3} + 0.9564\alpha^{*4} - 0.2537\alpha^{*5}) \tag{16}$$

given by Kakac et al. [52] from fitting the exact solutions of Shah & London [53] for different aspect ratios (α^{*}). In this case, the aspect ratio (α^{*}) equals the smallest dimension divided by the largest dimension. The Darcy friction factor depends on Eq. (16) and the gas Reynolds number (Re_G) as:

$$f = \frac{\overline{C}}{Re_G} \tag{17}$$

The theoretical pressure then follows the relation:

$$\left(\frac{dP}{dz}\right) = f\frac{\rho U_G^2}{2D_H} \tag{18}$$

where D_H equals the hydraulic diameter. The superficial gas velocity (U_G) equals the gas volumetric flow rate (Q_G) divided by the cross-sectional area (A_c).

Fig. 3 shows the comparison between the experimentally measured pressure drop and the theoretical value. The data fall within ±4.5% of the theoretical value for all experiments except for the two lowest. At 0.51 m/s and 0.85 m/s, the measurements fall below the theoretical value by 19% and 8.7%, respectively. The error bars for pressure in Fig. 3 account for the ±17.2 Pa accuracy of the pressure transducer. Utilizing the Kline-McClintock method on the equation $U_G = Q_G/A_c$, gives a velocity uncertainty of ±0.34 m/s at $U_G = 0.51$ m/s to ±0.43 m/s at $U_G = 5.5$ m/s. Conversely, the data for the hydrophilic case fell within ±4% for all experiments except for the two lowest; at 0.51 m/s and 0.85m/s, the measurements fall below the theoretical value by 17% and 7%, respectively (Fig. 3). Comparing the single-phase measurements between the hydrophilic and mixed-wettability cases, the measurements differ by less than ±1.5% relative to the hydrophilic case except differ by 2.6% and 1.75% for 0.51 m/s and 0.85 m/s. Therefore, the two cases agree well.

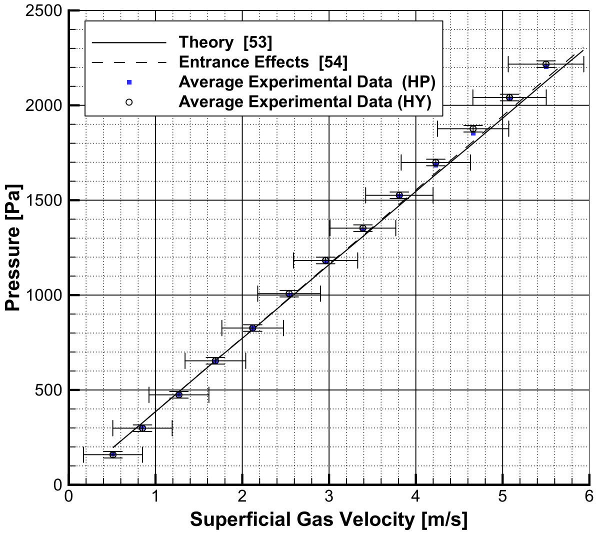

Fig. 3. Comparison of theoretical and experimental single-phase gas pressure drop versus superficial gas velocity for the hydrophillic (HP) and mixed-wettability (HY) cases.

The location of the first tap ($z = 0$) means that pressure measurements will include entrance effects. To account for the entrance effects, Shah defines an apparent Fanning friction factor [54] to replace Eq. (17). Comparing the experimental data to the correlation proposed by Shah, the data fall within ±3.7% for the mixed-wettability case and within ±3% for the hydrophilic case for all experiments except the two lowest that show negligible change (Fig. 3). Therefore, the inclusion of the entrance region has minimal influence on the measured pressure drop for either case.

5.2. Two-phase pressure results

The gas two-phase flow multiplier (ϕ_G^2) equals the ratio of the two-phase pressure drop to the single-phase pressure drop, representing the influence the liquid-phase has on the flow. In this study, the two-phase multiplier shows a decreasing trend as the superficial gas velocity increases (Fig. 4). ϕ_G^2 increases with increasing superficial liquid velocity at low superficial gas velocities but after $U_G = 2.96$ m/s, little change occurs in ϕ_G^2 at different U_L based on the average value. Each experimental data point represents a 30 min average of the pressure signal, after allowing 30 min for the flow to develop. At the highest superficial velocity, the data points represent 5 min averages after a 5 min development time. Comparing the measured two-phase flow multiplier between the mixed-wettability case and the hydrophilic case shows a significant increase in the two-phase flow multiplier. During the hydrophilic test at $U_L = 1 \times 10^{-2}$ m/s for $U_G = 0.51 - 1.27$ m/s water entered the downstream pressure tap and the results were excluded from the data set (Fig. 4d). While water entered the downstream tap only under the noted conditions in the hydrophilic case, the flow behavior in the mixed-wettability case caused water to enter the downstream tap in nearly all experiments. Based on measuring the single-phase pressure before the experiment, after the experiment, and after clearing the tap of water, the blocked tap resulted in an increase of the pressure from 0% up to 10%. However, a few experiments showed no water in the downstream tap. Those values followed the same trend as the other measurements, producing a two-phase flow multiplier higher than the hydrophilic case. In Fig. 4, error bars show the experimental uncertainty referenced to the average of the measured ϕ_G^2. The experimental uncertainty accounts for the accuracy of the pressure transducer of ±17.2 Pascals for both the single-phase and two-phase measurements determined by a Kline-McClintock uncertainty analysis. Additionally, the measured ϕ_G^2 values show a variability at a given test condition that falls outside the uncertainty of the measurement. While the varying influence of blocked pressure taps could account for differences in ϕ_G^2 up to 10%, the variation in ϕ_G^2 often exceeds 10%. Investigating the flow behavior will provide insight into the pressure variation.

5.3. Flow behavior

The interaction of air and water in a microchannel results in the formation of identifiable flow patterns. In the hydrophilic case, the flow formed as a stratified flow in which the water formed a film in contact with a side wall that occupied the entire height of the

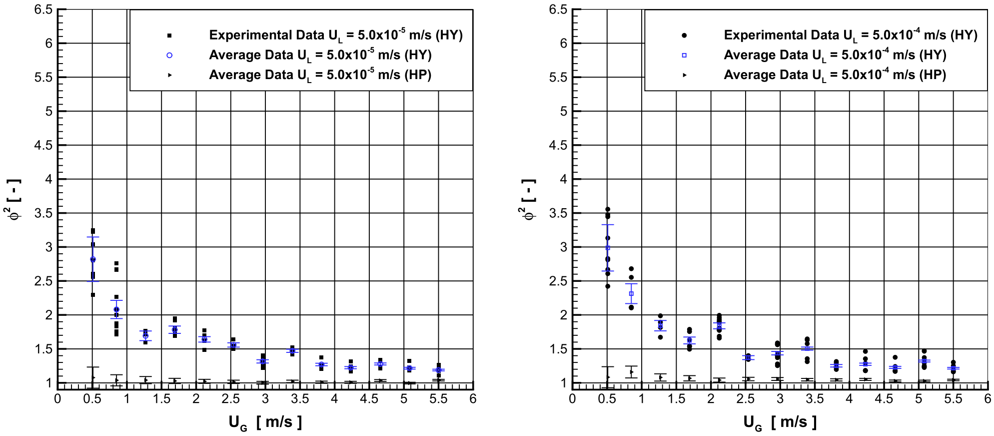

(a) $U_L = 5.0 \times 10^{-5}$ m/s.

(b) $U_L = 5.0 \times 10^{-4}$ m/s.

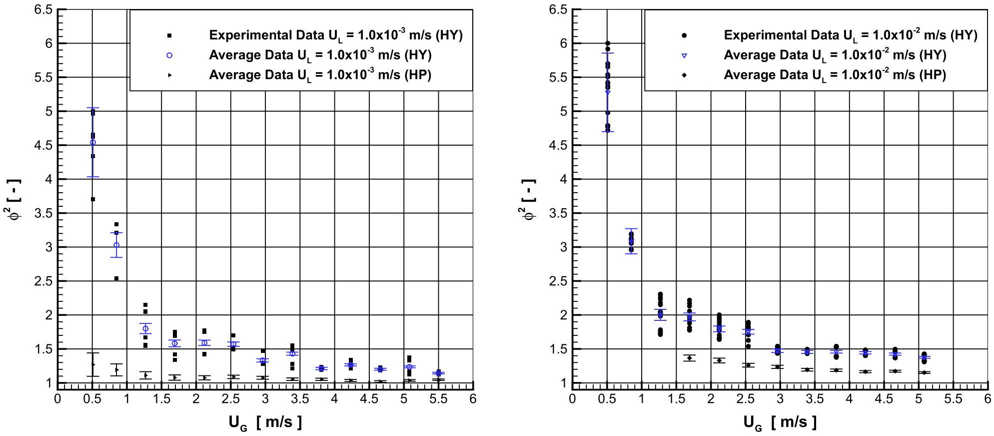

(c) $U_L = 1.0 \times 10^{-3}$ m/s.

(d) $U_L = 1.0 \times 10^{-2}$ m/s.

Fig. 4. Comparison between the mixed-wettability (HY) and hydrophilic (HP) microchannels for the pressure ratio versus superficial gas velocity.

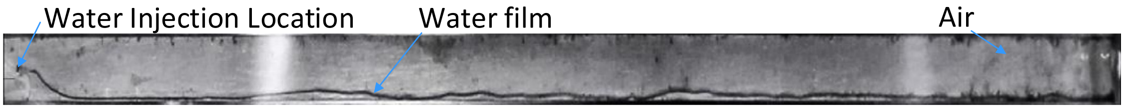

Fig. 5. Stratified flow for $U_L = 5.0 \times 10^{-4}$ m/s and $U_G = 1.27$ m/s, representative of the flow behavior in the hydrophilic channel experiments. The aspect ratio shown does not represent the true aspect ratio.

channel but only part of the channel width. Stratified flow formed for the range of test conditions, where the thickness of the water film (Fig. 5) changed with test conditions [cf. 11]. In the mixed-wettability case, flow visualization revealed multiple flow patterns (Fig. 6) over the range of test conditions, fundamentally different than the stratified flow visualized in the hydrophilic case.

Fig. 6 demonstrates the observed flow patterns in this study presented as a top-down view. In the figure for a given pair of U_L and U_G, a single frame denotes a stationary behavior relative to the frame rate, while multiple frames show the periodic behavior of the flow occurring at the stated test conditions. The stationary behavior refers to the fact that the flow pattern remains unchanged between frames but water still flows through the channel. The left side of each frame corresponds to the water injection location and the frame ends just before the location of the downstream pressure tap.

Under the conditions of superficial liquid velocity (U_L) equal to 5.0×10^{-5} m/s and superficial gas velocity (U_G) equal to 0.51 m/s, elongated droplets form and eventually contact the channel walls. The formation of a second droplet occurs before the previous water clears. The water propagates downstream, leaving residual water on the channel walls, with another droplet forming behind (Figs. 6a & 7a). The residual water during $U_L = 5.0 \times 10^{-4}$ m/s and $U_G = 0.51$ m/s flow (Fig. 6d) remains relatively unchanged as the droplets form. At the two highest superficial liquid velocities ($U_L = 1.0 \times 10^{-3}$ & $U_L = 1.0 \times 10^{-2}$ m/s) at $U_G = 0.51$ m/s, the flow forms as a stratified flow with entrained air bubbles (Figs. 6g and j & 7b), similar to the flow pattern seen by Choi et al. [17].

As the superficial gas velocity increases, the flow takes on the characteristics of a rivulet flow. A rivulet consists of a thin film of water moving along the bottom surface of the channel but not contacting the side walls nor the top of the channel. The dashed lines in Fig. 6 represent the rivulet. Although drawn as straight lines, the rivulet tends to wind along the channel. Barajas & Panton [19] noted a similar behavior in a 1.6 mm diameter tube. At the end of the rivulet, drops periodically form and break off, leading to a

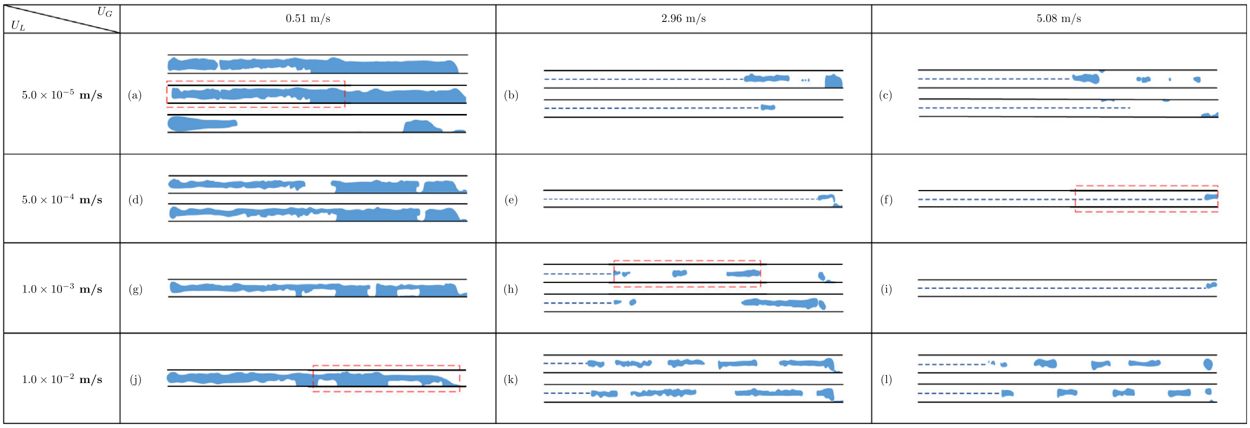

Fig. 6. Observed flow patterns in a mixed-wettability microchannel (Flow from left to right; water indicated in blue). The regions highlighted with a dashed red line correspond to the images in Fig. 7.

series of confined droplets (Figs. 6h, k, and l). The tests of $U_L = 1.0 \times 10^{-2}$ at $U_G = 2.96$ & 5.08 m/s show the droplet length decreases with increasing superficial gas velocity (Figs. 6k and l). Jose & Cubaud [55] identified a similar behavior for water-silicon oil flows (liquid-liquid flow) in a 250 μm square microchannel; the water droplets formed spherical or bullet shapes depending on the capillary number with nearly uniform spacing. Conversely, in this work the confined water droplets have irregular shape and spacing (Fig. 7d). Additionally, the location of the rivulet end can change location and upon break-up of the drop leave residual water in the channel (Figs. 6b and c).

The rivulet in several experiments (Figs. 6e, f, and i) extended nearly the entire observed length of the channel, terminating in a stationary drop (Fig. 7c). Repetition of the experiments shown in Figs. 6e, f, and i produced the same flow behavior as shown. However, at $U_L = 1.0 \times 10^{-3}$ m/s with $U_G = 5.50$ m/s, the flow behaved similar to the flow shown in Fig. 6h. Between the mixed-wettability and the hydrophilic microchannel, only the wetting properties of the base changed. Thus, changing the wetting properties of the materials changes the flow behavior.

5.3.1. Variability of flow behavior

Flipo et al. [56] noted multiple flow patterns occurred for the same test conditions and could even change during a given test in a hydrophobic channel. In this work, measurements of the gas two-phase flow multiplier show several cases in which the measurements fell outside the range of uncertainty (Fig. 4). Visualization of the flow behavior demonstrates the pressure change corresponds to a change in the flow behavior.

Under fixed test conditions the flow can change fundamentally between different tests (Fig. 8). For example, at $U_L = 5 \times 10^{-4}$ m/s for $U_G = 2.12$ m/s, a long rivulet formed terminating in a stationary drop in one case (Fig. 8a), while a shorter rivulet formed producing a series of confined droplets in another case (Fig. 8b). This produced ϕ_G^2 values of 1.86 and 1.67, respectively. The time trace of the pressure signal demonstrates the nature of the two flows (Fig. 8c). In the case of Test 2, the pressure signal shows an oscillating pressure corresponding to the movement of the droplets while the Test 1 shows little pressure variation in time. The pressure oscillation for Test 1 corresponds to the characteristic frequency of the syringe pump. Additionally, the number and length of

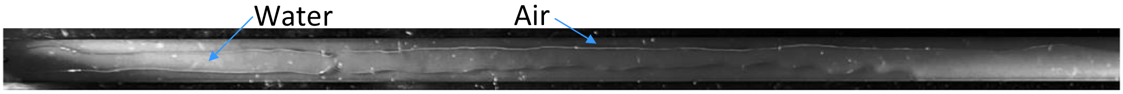

(a) Elongated-drop flow (figure 6a)

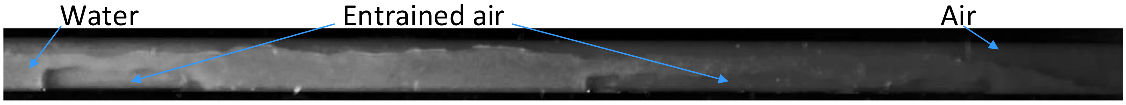

(b) Stratified flow with entrainment (figure 6j)

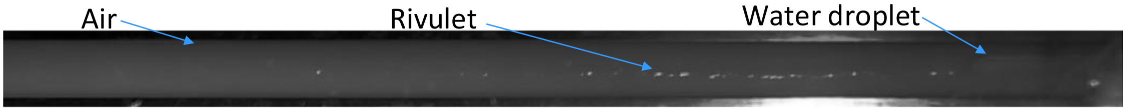

(c) Stationary rivulet flow (figure 6f)

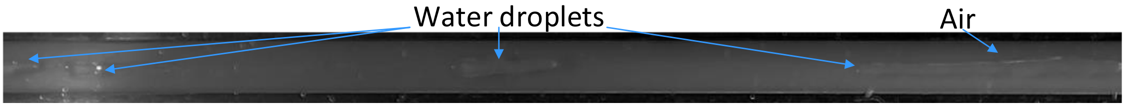

(d) Dynamic rivulet flow (figure 6h)

Fig. 7. Images of the flow patterns corresponding to the highlighted regions of Fig. 6 where the flow goes from left to right.

(a) $\phi_G^2 = 1.86$ (Test 1).

(b) $\phi_G^2 = 1.67$ (Test 2).

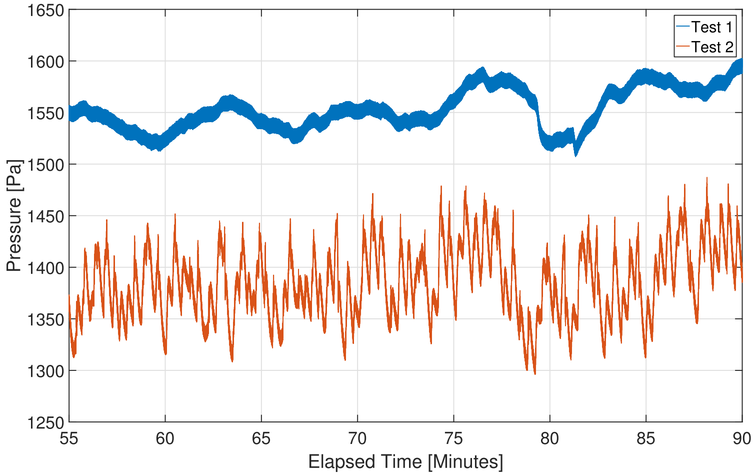

(c) Pressure signals.

Fig. 8. Variable flow behavior at $U_G = 2.12$ m/s and $U_L = 5.0 \times 10^{-4}$ m/s. In figures (a) and (b), blue indicates the water and the flow moves from left to right.

droplets changes in Test 2 (Fig. 8b) resulting in varying peak-to-peak pressure values. Therefore, under a given set of test conditions, the flow can take on different characteristics, which leads to differing ϕ_G^2 values.

5.4. Comparison of existing experimental results

Section 2.1 discussed existing experimental results for how the two-phase pressure changes when comparing hydrophilic to hydrophobic microchannels. As Fig. 4 illustrates, the mixed-wettability microchannel produces a higher two-phase pressure than the hydrophilic microchannel that differs only by the contact angle of the base. This trend agrees with the results of Cho & Wang [15], Phan et al. [16], and Rapolu & Son [18]. However, Stevens et al. [12], Wang et al. [10], and Choi et al. [17] found the opposite trend when comparing a hydrophobic to hydrophilic microchannel where the hydrophilic microchannel had a larger two-phase pressure than a hydrophobic channel. Additionally, Lu et al. [8] found that the trend changed for the same configuration with an increase in superficial liquid velocity while Wang et al. [14] found the two-phase pressure in the hydrophilic case fell between the pressure measurements of a hydrophobic and superhydrophobic case. Achieving an optimal design requires understanding how design choices impact the design goals and thus necessitates clarifying the inconsistency between the presented works. This section focuses on the careful consideration of experimental parameters to identify consistent behaviors of the two-phase pressure between existing works.

Different works will primarily differ in terms of test conditions, scales, and levels of hydrophobicity. Consider first the liquid-only Reynolds number (Re_{lo}) and the level of hydrophobicity. Fig. 9 compares the range of hydrophobicity (contact angle) to the liquid-only Reynolds number based on differentiating between mixed-wettability (Fig. 9a) and homogeneous (Fig. 9b) microchannels. The trend of Wang et al. [14] and Phan et al. [16] conflict with that of Stevens et al. [12] in the mixed-wettability case, while in the homogeneous case the experiments of Wang et al. [10] conflict with Rapolu & Son [18]. The results of Lu et al. [8] both agree and disagree with the current work. Considering both the mixed-wettability and homogeneous experiments together would lead to further disagreement. Thus, the comparison indicates that simply looking at the level of hydrophobicity and Re_{lo} does not resolve the differences between experiments without further refinement of the analysis beyond the first refinement of distinguishing between mixed-wettability and homogeneous microchannels.

A second distinction arises by limiting the comparison to similar experiments. The works illustrated in Fig. 9 conducted experiments of adiabatic two-phase flow in a single channel with the exception of Lu et al. [8] and Phan et al. [16]. The apparatus of Lu et al. consisted of eight parallel channels and Phan et al. conducted flow boiling experiments. As the two experiments differ fundamentally from the other works, the analysis does not consider them further. Removing the two experiments from Fig. 9a would leave only a conflicting behavior between Wang et al. [14] and Stevens et al. [12] in the mixed-wettability case.

With an inconsistency remaining between Wang et al. [14] and Stevens et al. [12], other experimental conditions may clarify the trend. At small scales surface tension becomes dominant and thus the Capillary number may influence the result. The liquid Capillary number (Ca_L) relates the viscous forces to the surface tension forces of the liquid as:

$$Ca_L = \frac{\mu_L U_L}{\sigma} \tag{19}$$

where σ stands for surface tension and U_L the liquid superficial velocity. Fig. 10 compares the trend of the two-phase pressure (ΔP_{tp}) with contact angle to the liquid Capillary number for the mixed-wettability (Fig. 10a) and homogeneous (Fig. 10b) microchannels. Similar to the liquid-only Reynolds number, the liquid Capillary number did not reorganize the experimental results into a consistent behavior for the homogeneous experiments. Conversely, using the Ca_L re-organizes the mixed-wettability data into a consistent trend (Fig. 10a). The two-phase pressure increases for a mixed-wettability microchannel relative to a hydrophilic microchannel for this work and the work of Cho & Wang [15], fall-

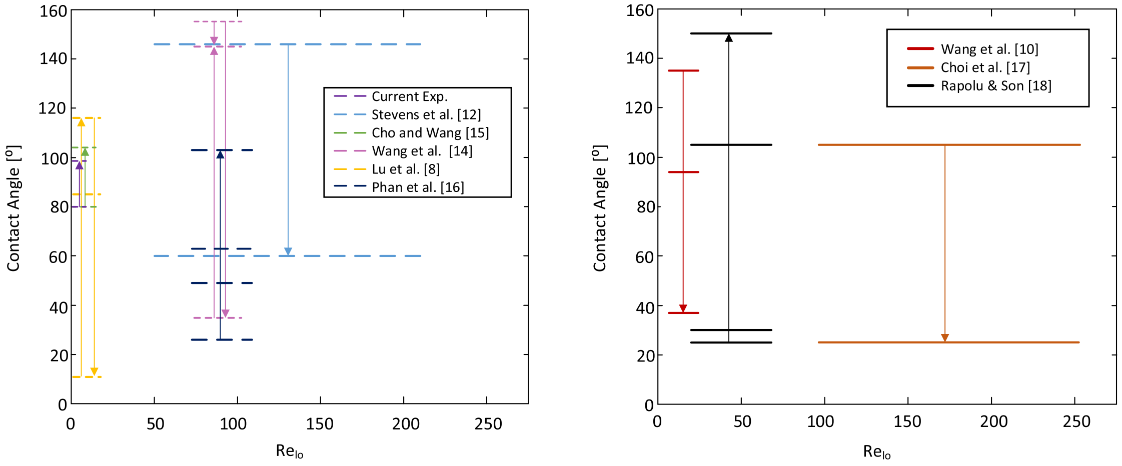

(a) Mixed-wettability experiments.

(b) Homogeneous experiments.

Fig. 9. Contact angle versus liquid-only Reynolds number (arrows indicate the direction of the pressure change, double lines indicate inconsistent trends).

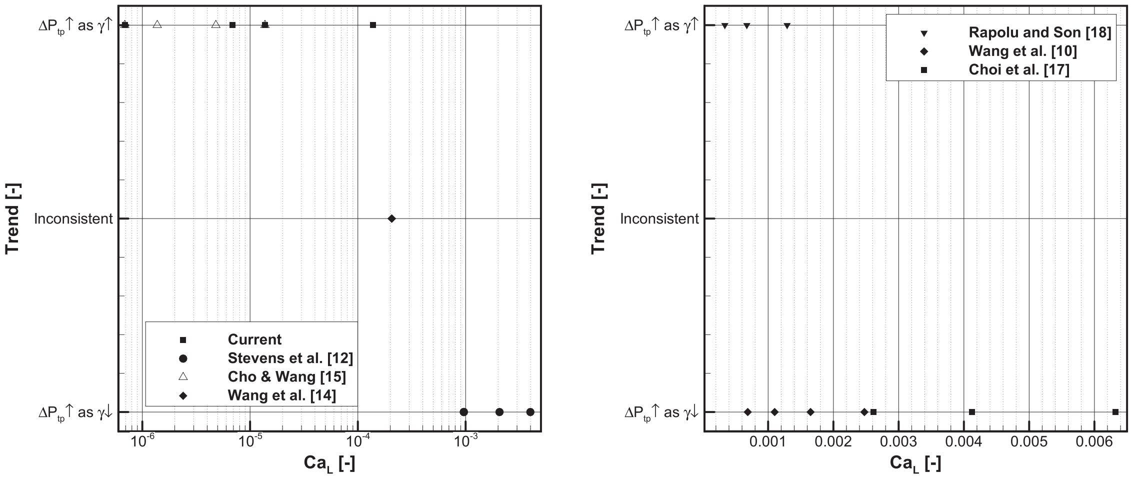

(a) Mixed-wettability experiments.

(b) Homogeneous experiments.

Fig. 10. Trend of the two-phase pressure (ΔP_{tp}) with contact angle (γ) versus liquid Capillary number. Arrows on y-axis indicate increasing (↑) or decreasing (↓) behavior.

ing in a Ca_L range of 6.88×10^{-7} to 1.38×10^{-4}. For Stevens et al. [12], the two-phase pressure decreased for a mixed-wettability microchannel relative to a hydrophilic microchannel in a Ca_L range of 9.63×10^{-4} to 3.99×10^{-3}. The inconsistent trend of Wang et al. [14] fell in-between with a Ca_L of 2.06×10^{-4}. The analysis could suggest that a critical liquid Capillary number falling between 1.38×10^{-4} to 9.63×10^{-4} exists for single mixed-wettability microchannels with adiabatic flow.

The superhydrophobic nature of channels of Wang et al. [14] and Stevens et al. [12] compared to the hydrophobic characteristic of the current work and that of Cho & Wang [15] discussed in Fig. 10a requires further discussion. Superhydrophobic surfaces in a Cassie state allow for a slip boundary as water moves over air trapped between surface structures [cf. 57] such as the rib-cavity structure utilized by Stevens et al. [12]. Slip at the wall will reduce friction compared to a no-slip boundary, leading to a lower pressure drop in a channel. Water can also fill the surface structures—termed a Wenzel state—which will then produce negligible slip, even with a high contact angle [cf. 58]. Simple hydrophobic surfaces do not have noticeable slip. Consequently, the trend illustrated in Fig. 10a could result from the introduction of different physics (slip) for Stevens et al. [12] and the inconsistent trend of Wang et al. [14] as a result of comparing PTFE (hydrophobic, no-slip) to a superhydrophobic surface. Therefore, the analysis must consider a third distinction between hydrophobic and superhydrophobic due to the different physics. Thus, the critical Capillary number does not necessarily apply.

By differentiating between mixed-wettability channels & homogenous microchannels, hydrophobic & superhydrophobic surfaces, and by isolating the comparison to adiabatic flow in a single channel, the behavior of existing literature becomes consistent. Based on the current work combined with the works of Cho & Wang [15] and the PTFE data of Wang et al. [14], the two-phase pressure in a mixed-wettability microchannel will increase relative to a hydrophilic microchannel independent of Re_{lo}, Ca_L, and the level of hydrophobicity. For the superhydrophobic surfaces of Stevens et al. [12] and Wang et al. [14], the two-phase pressure in a mixed-wettability microchannel will decrease relative to a hydrophilic microchannel independent of the analyzed parameters. Analyzing the hydraulic diameters between the experiments to represent scale leads to an independence of scale under the same restrictions. In the case of a homogeneous microchannel, the works of Rapolu & Son [18], Wang et al. [10], and Choi et al. [17] the results become consistent with hydraulic diameter but not with Re_{lo} nor Ca_L—albeit the analysis consists of three points and could result from coincidence. With a limited number of data, future work will need to add homogeneous, hydrophobic mixed-wettability, and superhydrophobic mixed-wettability microchannel experiments to ensure the consistency remains. Particularly, since superhydrophobic channels can obtain either a Cassie or Wenzel state with different physics, a critical Capillary number may exist where the state transitions.

5.5. Correlating the experimental data with existing two-phase pressure models

The previous sections discussed the trend in the two-phase pressure drop and the behavior of the flow. This section will analyze how the existing two-phase pressure models discussed in Section 3 predict the experimental data in a mixed-wettability microchannel.

5.5.1. Statistical method for model comparison

The statistical method for assessing the two-phase pressure models follows the method of Lewis & Wang [11] relying on the mean absolute percent error ($|\bar{e}_{\%}|$), the root-mean-square percent error ($\sigma_{\%}$), the mean error ($\bar{e}$), mean percent error ($\bar{e}_{\%}$), and the root-mean-square error (σ_e). The scale dependent statistical quantities rely on the error (δP_i) defined as the two-phase pressure drop calculated from the model ($\Delta P_{pre,i}$) minus the experimentally measured pressure drop ($\Delta P_{exp,i}$) for the *ith* experimental datum. Similarly, the scale independent statistical quantities rely on the percent error ($\delta^* P_i$) defined as the error (δP_i) divided by $\Delta P_{exp,i}$. Thus the statistical quantities have the definitions:

$$|\bar{e}_{\%}| = \frac{1}{n}\sum\nolimits_{i=1}^{n} |\delta^* P_i| \tag{20}$$

$$\sigma_{\%} = \left(\frac{1}{n}\sum\nolimits_{i=1}^{n} (\delta^* P_i)^2\right)^{0.5} \tag{21}$$

$$\bar{e} = \frac{1}{n}\sum\nolimits_{i=1}^{n} \delta P_i \tag{22}$$

$$\bar{e}_{\%} = \frac{1}{n}\sum\nolimits_{i=1}^{n} \delta^* P_i \tag{23}$$

$$\sigma_e = \left(\frac{1}{n}\sum\nolimits_{i=1}^{n} (\delta P_i)^2\right)^{0.5} \tag{24}$$

where n equals the number of data points.

Figures plotting the experimentally measured two-phase pressure (ΔP_{exp}) versus the value predicted by the two-phase pressure models (ΔP_{pre}) aid in understanding the statistics. The solid line in Figs. 11–16 represent a perfect prediction for the two-phase pressure measurements by the model. Each figure shows the data for the four superficial liquid velocities tested to determine trends of the prediction. Data failing above the solid line indicates the model

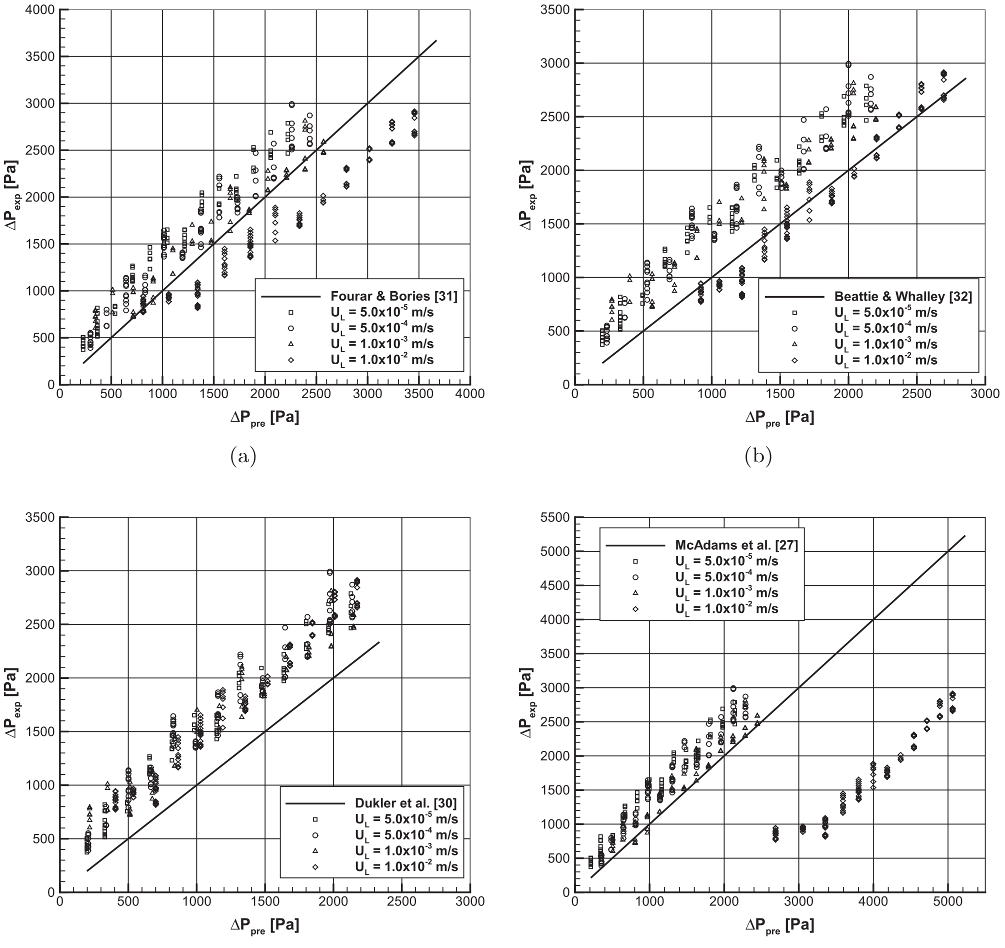

(a) (b)

(c) (d)

Fig. 11. Comparison between the mixed-wettability experimental data and the predicted two-phase pressure drop for the homogeneous flow models.

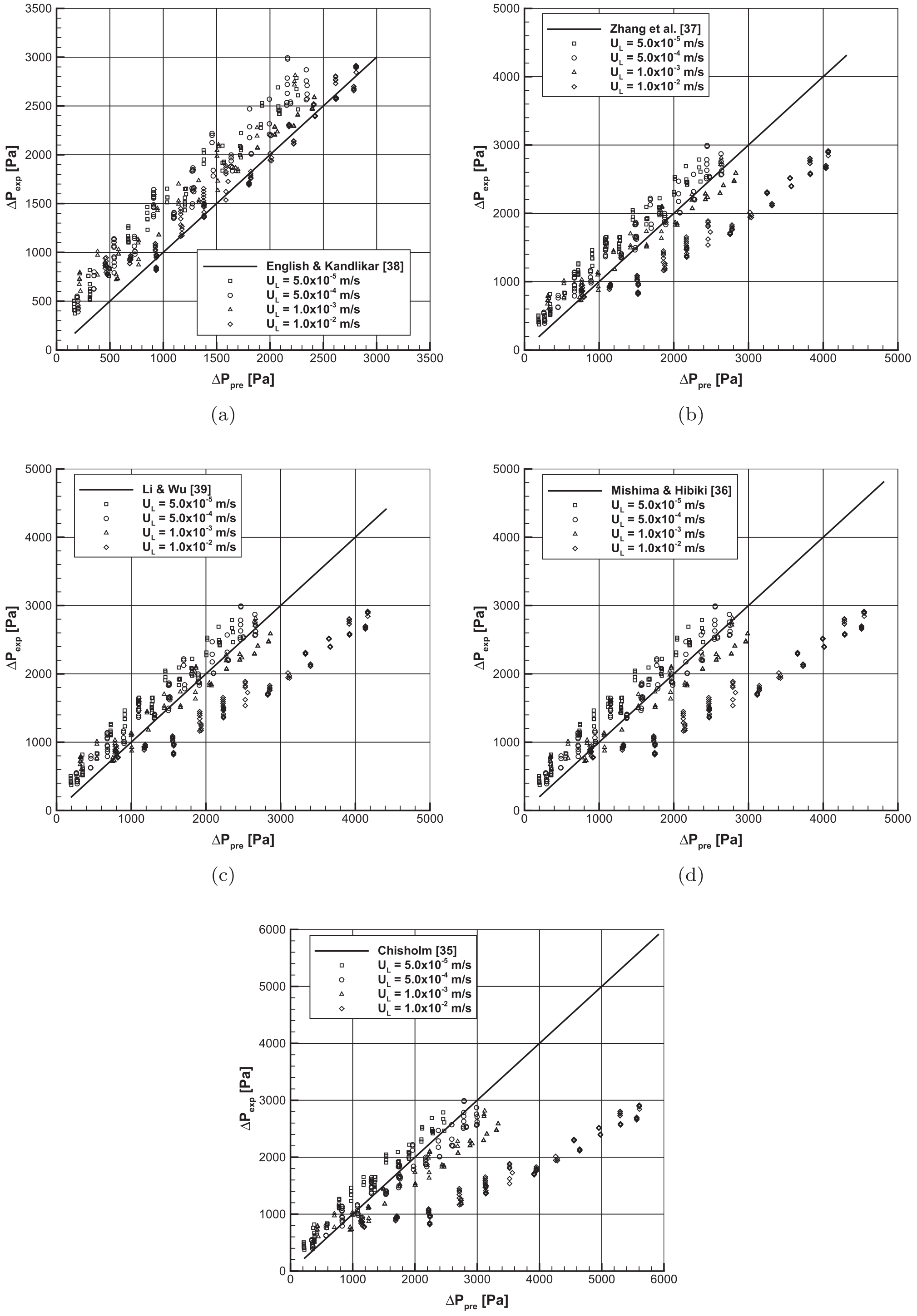

(a)

(b)

(c)

(d)

(e)

Fig. 12. Comparison between the mixed-wettability experimental data and the predicted two-phase pressure drop for separated flow models with constant *C*-values.

under-predicts the experimental measurements whereas data below the solid line indicates an over-prediction.

5.5.2. Comparison to homogeneous flow models

Of the selected homogeneous flow models, the model of Fourar & Bories [31] outperforms the other models (Table 4). Initially, the model of Fourar & Bories under-predicts the experimental data (Fig. 11a) with a $\bar{e} = -378$ Pa at $U_L = 5.0 \times 10^{-5}$ m/s and decreasing as U_L increases to a minimum mean error of -157.5 Pa at $U_L = 1.0 \times 10^{-3}$ m/s. At $U_L = 1.0 \times 10^{-2}$ m/s, the model of Fourar & Bories over-predicts the experimental data with a $\bar{e} = 402.5$ Pa. Conversely, the model of Beattie & Whalley [32] better predicts the two-phase pressure at $U_L = 1.0 \times 10^{-2}$ m/s with a mean error of 46.5 Pa while under-predicting the remaining data sets (Fig. 11b). The under-prediction does not have a decreasing trend in the mean error, with values of $-438.5, -485$, and -404.6 for

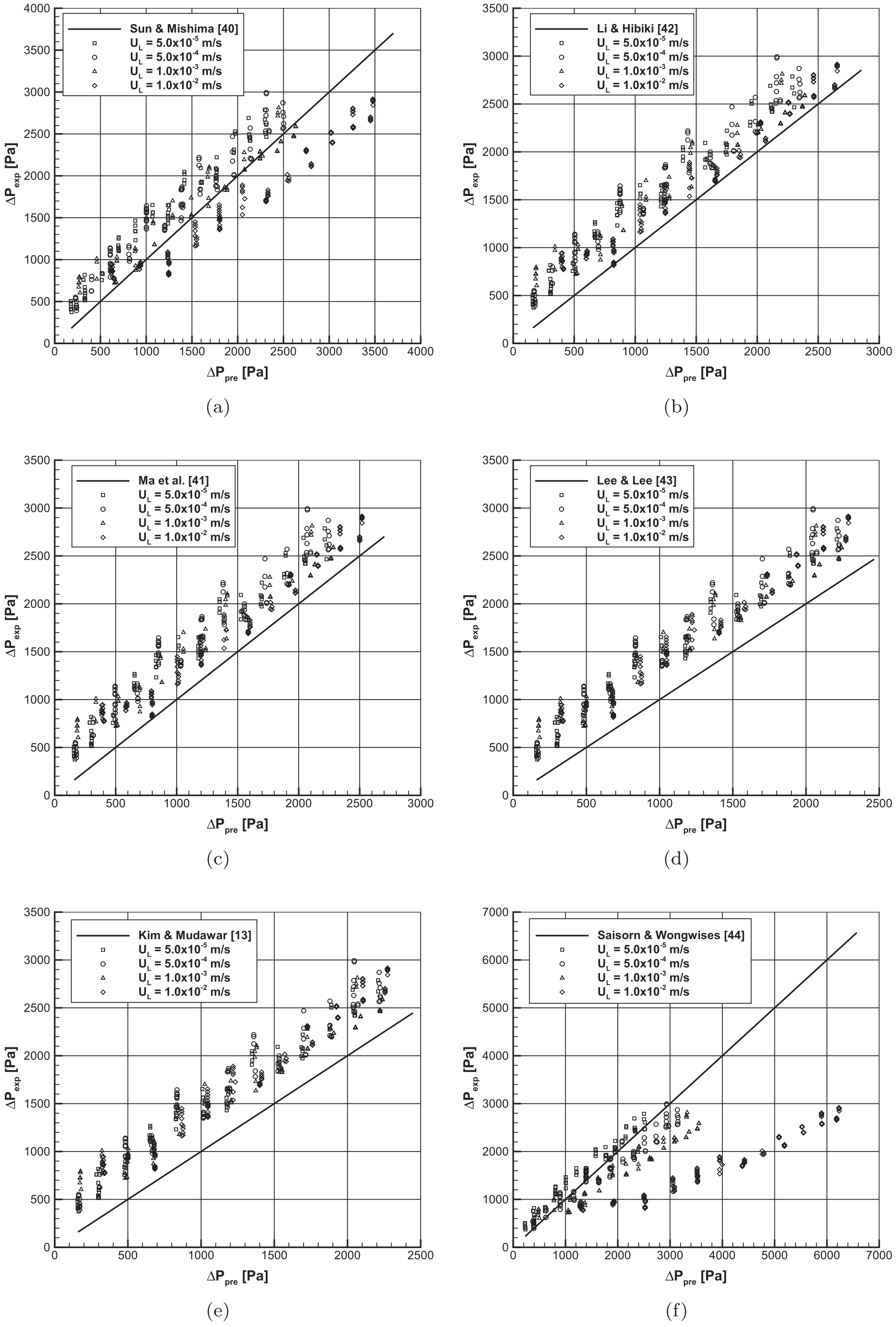

(a) (b)

(c) (d)

(e) (f)

Fig. 13. Comparison between the mixed-wettability experimental data and the predicted two-phase pressure drop for separated flow models with flow dependent *C*-values.

superficial liquid velocities from 5.0×10^{-5} to 1.0×10^{-3} m/s, respectively. This leaves the majority of the data clustered away from the prediction (Fig. 11b). The model of Dukler et al. [30] shows the same trend for all the superficial liquid velocities (Fig. 11c) with means errors of $-441, -511, -457.6$, and -474.5 Pa for U_L from 5.0×10^{-5} to 1.0×10^{-2} m/s, respectively. The remaining models in Table 4 follow the trend of McAdams et al. [27] in which the model significantly over-predicts one or more of the U_L data sets (Fig. 11d). Based on the trends, the model of Dukler et al. produces too low of a two-phase viscosity, the viscosity model of Beattie & Whalley does not change rapidly enough at low U_L, while the model of Fourar & Bories changes too quickly at higher U_L.

5.5.3. Comparison to separated flow models

The separated flow model comparison consists of three categories: models producing constant *C*-values, models that produce *C*-values varying with test conditions, and models that researchers have proposed for hydrophobic microchannels. The model of English & Kandlikar [38] predicts the experimental data better than the

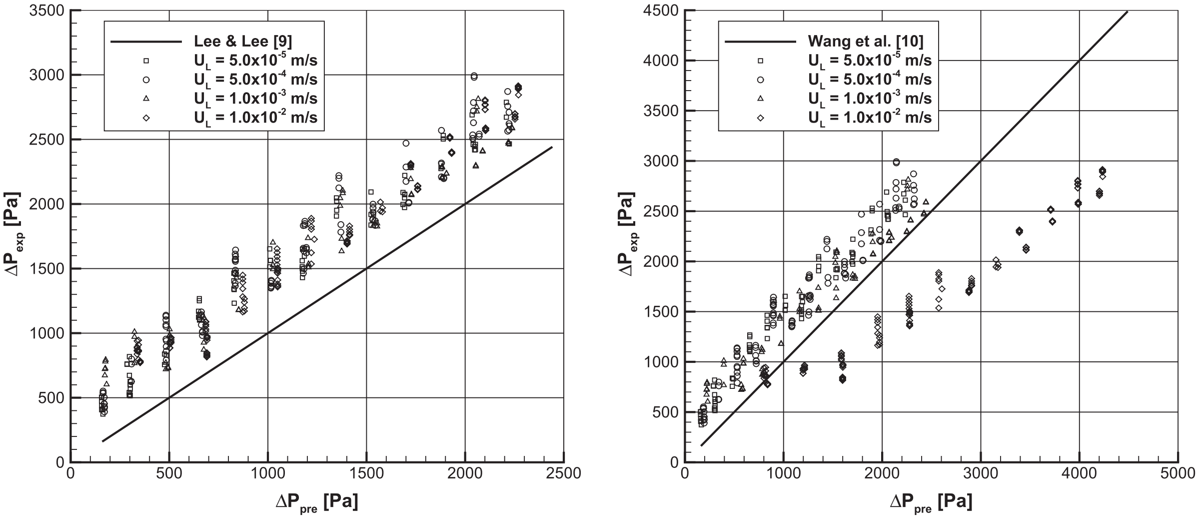

(a) (b)

Fig. 14. Comparison between the mixed-wettability experimental data and the predicted two-phase pressure drop for the separated flow models modified for hydrophobic microchannels.

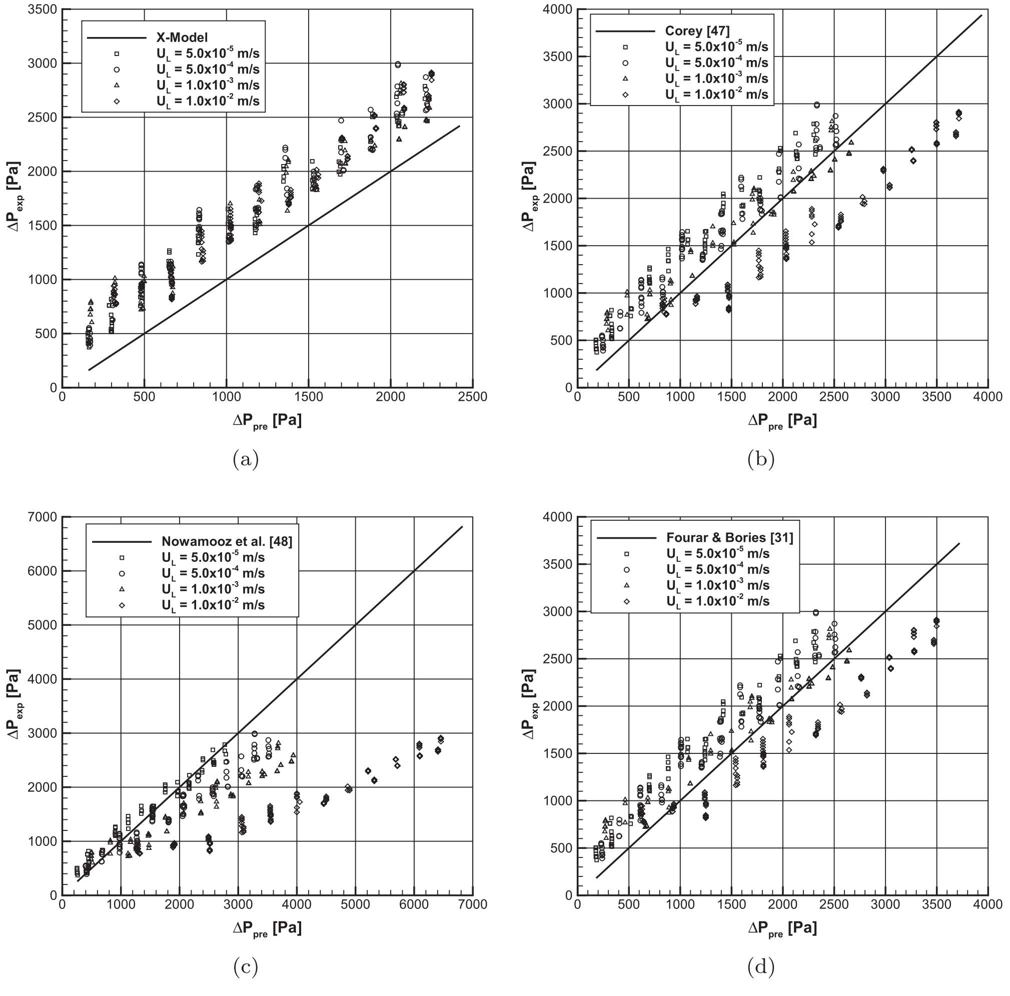

(c) (d)

Fig. 15. Comparison between the mixed-wettability experimental data and the predicted two-phase pressure drop for the relative permeability models with modeled saturation.

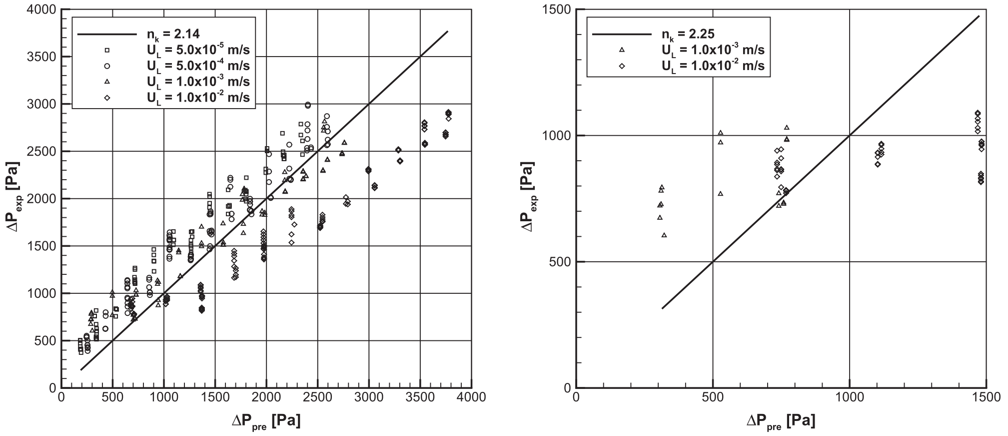

(a) Complete data set.

(b) Entrained-stratified flow.

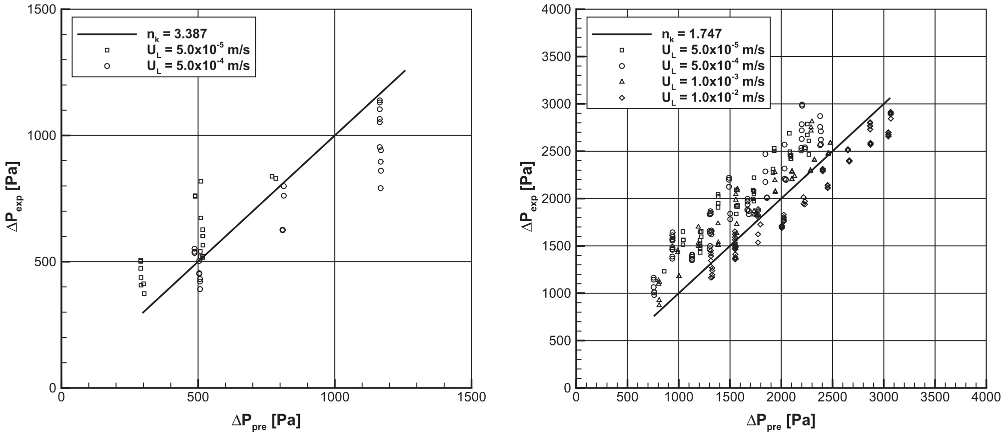

(c) Elongated droplet flow.

(d) Rivulet Flow.

Fig. 16. Comparison between different subsets of the mixed-wettability experimental data and the predicted two-phase pressure drop for optimized n_k values in the two-fluid model.

Table 4
Overall error statistics of the homogeneous flow models for the mixed-wettability case.

	$\bar{e}$ (Pa)	σ_e (Pa)	$\bar{e}_{\%}$	$\sigma_{\%}$	$\lvert\bar{e}_{\%}\rvert$
Fourar & Bories [31]	−29.9	391.7	−5.1%	26.9%	23.1%
Beattie & Whalley [32]	−262.5	389.4	−17.8%	28.9%	23.8%
Dukler et al. [30]	−474.1	500	−32.8%	35.2%	32.8%
McAdams et al. [27]	637.4	1414	44.4%	106%	73.7%
Lin et al. [29]	1709	3069	124%	243%	147%
Awad & Muzychka [33]	2469	4179	167%	287%	182%
Cicchitti et al. [28]	18090	26681	1075%	1417%	1075%

Table 5
Overall error statistics of separated flow models producing constant *C*-values.

	$\bar{e}$ (Pa)	σ_e (Pa)	$\bar{e}_{\%}$	$\sigma_{\%}$	$\lvert\bar{e}_{\%}\rvert$
English & Kandlikar [38]	−296.6	340.2	−21.7%	29.0%	22.7%
Zhang et al. [37]	152.7	570.4	4.1%	35.0%	28.9%
Li & Wu [39]	186	607.7	6.1%	36.7%	30.0%
Mishima & Hibiki[36]	314	759.3	13.9%	43.9%	34.5%
Chisholm [35]	668	1208	35.4%	67.4%	50.2%

Table 6
Overall error statistics of separated flow models using correlations producing variable *C*-values.

	$\bar{e}$ (Pa)	σ_e (Pa)	$\bar{e}_{\%}$	$\sigma_{\%}$	$\lvert\bar{e}_{\%}\rvert$
Sun & Mishima [40]	−45.2	383.4	−8.0%	28.0%	23.7%
Li & Hibiki[42]	−329	370	−25.7%	31.6%	25.8%
Ma et al. [41]	−378	411	−28.3%	33.1%	28.3%
Lee & Lee [43]	−447	470	−32.5%	36.2%	32.5%
Kim & Mudawar [13]	449	472	−32.6%	36.3%	32.6%
Saisorn & Wongwises [44]	880	1482	48.3%	82.2%	60.2%

other constant *C*-value correlations (Table 5). The correlation of English & Kandlikar under-predicts the experimental data with mean errors of −393.6, −402.6, −304.6, and −96.8 Pa for U_L from 5.0×10^{-5} to 1.0×10^{-2} m/s, respectively. Statistically, the correlations of Mishima & Hibiki [36], Zhang et al. [37], and Li & Wu [39] deviate less than that of English & Kandlikar in the range of $U_L = 5.0 \times 10^{-5}$ to 1.0×10^{-3} m/s. The correlation of Chisholm [35] produces smaller mean errors for the two lowest superficial liquid velocities. However, the correlations over-predict the experimental data at $U_L = 1.0 \times 10^{-2}$ m/s (Fig. 12).

The analysis of the correlations where the *C*-value varies with test conditions demonstrates no significant improvement by allowing the *C*-value to vary with test conditions. Of the selected relations, the correlation of Sun & Mishima [40] produces the lowest mean absolute percent error (Table 6) of 23.7%. The correlation initially under-predicts the experimental data with a decreasing mean error of −362.1, −299.1, −153.6 Pa as the superficial water velocity increases from $U_L = 5.0 \times 10^{-5}$ to 1.0×10^{-3} m/s. For the highest superficial water velocity, the correlation over-predicts

Table 7
Overall error statistics of separated flow models modified for hydrophobic channels.

	$\bar{e}$ (Pa)	σ_e (Pa)	$\bar{e}_{\%}$	$\sigma_{\%}$	$\lvert\bar{e}_{\%}\rvert$
Lee & Lee [9]	−488.1	471.2	−32.5%	36.1%	32.5%
Wang et al. [10]	80.3	677.6	−0.8%	42.1%	36.7%

the data with a mean error of 347 Pa (Fig. 13a). While deviating further in magnitude than the correlation of English & Kandlikar [38] at $U_L = 1.0 \times 10^{-2}$ m/s, the relation of Sun & Mishima [40] produces smaller mean errors for the other superficial liquid velocities. Consequently, the correlation of Sun & Mishima has a slightly lower root-mean-square percent error than the relation of English & Kandlikar (28.0% compared to 29.0%). Although the two correlations produce different trends in correlating the experimental data, the similar statistics mean the two correlations have equal validity in correlating the data.

The remaining constant *C*-value correlations generally under-predict the experimental data (Fig. 13). The relations of Lee & Lee [43] and Kim & Mudawar [13], produce similar mean errors of $-419, -486, -426$, and -450 Pa for the range of superficial liquid velocities of 5.0×10^{-5} to 1.0×10^{-2} m/s (Fig. 13d and e). The correlations of Li & Hibiki [42] and Ma et al. [41] produce similar results, except achieve minimum mean errors of −224 Pa and −287 Pa, respectively, at $U_L = 1.0 \times 10^{-2}$ m/s (Fig. 13b and c). The correlation proposed by Saisorn & Wongwises [44] only under predicts the $U_L = 5.0 \times 10^{-5}$ m/s data with a $\bar{e} = -229.5$ Pa. As the superficial liquid velocity increases the mean error increases from 135 Pa to 2163 Pa (Fig. 13f).

Analyzing the relations derived for hydrophobic channels provides interesting results (Table 7). The correlation of Lee & Lee [9] under-predicts the experimental data (Fig. 14a) with mean errors of $-419, -486, -427$, and -447 as U_L increases from 5.0×10^{-5} to 1.0×10^{-2} m/s, respectively. This produces nearly the same statistics as the original relation for hydrophilic channels [43, Lee & Lee] shown in Fig. 13d. Additionally, the relation of Saisorn & Wongwises [44], which modified the exponents of Lee & Lee [43], did not accurately predict the two-phase pressure in this experiment. Therefore, adjusting the parameters in the relation of Lee & Lee [43] tends to have specific applicability.

As Fig. 14b illustrates, the relation of Wang et al. [10] produces varying trends dependent on the superficial liquid velocity. From $U_L = 5.0 \times 10^{-5}$ to 1.0×10^{-3} m/s, the correlation under-predicts the data with mean errors of $-419, -486$, and -426.8 Pa, respectively. At $U_L = 1.0 \times 10^{-2}$ m/s, the correlation over-predicts the experimental data with a mean error of 847 Pa. As a result, modifying the *C*-value with a function of the contact angle does not improve the model's ability to predict the experimental work, compared to the predictive accuracy of the other relations.

5.5.4. Comparison to relative permeability models

While the imaging technique provides qualitative behavior of the flow, the method did not provide saturation measurements. As the relative permeability models require saturation values, the assessment of the models relies on a saturation model (Eq. (15)). Calculating the saturation for the X-model, the model of Corey [47], and Nowamooz et al. [48] uses n_k values of 1, 2, and 3.05, respectively. The model of Fourar & Bories [31] has an accompanying saturation model. The assessment does not include the models of Chen et al. [49], Fourar & Lenormand [50], or Huang et al. [51], as a single n_k value cannot simplify the relations, which prevents using the saturation model.

The combination of the saturation and relative permeability models of Fourar & Bories [31] performs statistically (Table 8) similar to the relation of Sun & Mishima [40] and the homogeneous model also proposed by Fourar & Bories. Initially, the model under-predicts the experimental data with mean errors of $-360.3, -293.5$, and -145.8 Pa for $U_L = 5.0 \times 10^{-5}$ to 1.0×10^{-3} m/s, respectively. Conversely, at $U_L = 1.0 \times 10^{-2}$ m/s the model over-predicts the experimental data with a mean error of 365.7 Pa (Fig. 15d). The model of Corey [47] follows a similar trend. The model first under-predicts the experimental data with mean errors of $-360, -283.7$, and -126 Pa for $U_L = 5.0 \times 10^{-5}$ to 1.0×10^{-3} m/s, respectively. The model over-predicts the data set of $U_L = 1.0 \times 10^{-2}$ m/s with a mean error of 365.7 Pa (Fig. 15b).

Table 8
Overall error statistics of the relative permeability models based on modeled saturation.

	$\bar{e}$ (Pa)	σ_e (Pa)	$\bar{e}_{\%}$	$\sigma_{\%}$	$\lvert\bar{e}_{\%}\rvert$
Fourar & Bories [31]	−38.8	386.6	−7.7%	28.1%	23.7%
Corey [47]	50.1	473.7	−1.3%	32.2%	27.2%
X-Model	−457.6	480.3	−33.2%	36.8%	33.2%
Nowamooz et al. [48]	1019	1568.5	55.8%	85%	63.6%

The model of Nowamooz et al. [48] and the X-model provide bounds for the optimized n_k value of the data. The model of Nowamooz et al. primarily over-predicts the measurements with mean errors of 327, 685.5, and 2236 Pa respective to the superficial liquid velocities of 5.0×10^{-4} to 1.0×10^{-2}. The model under-predicts the measurements at $U_L = 5.0 \times 10^{-5}$ m/s with a mean error of −87 Pa (Fig. 15c). Conversely, the X-model under-predicts all the experimental results, with nearly consistent mean errors of $-419.5, -488, -429$, and -470 Pa from low to high superficial liquid velocity (Fig. 15a). Based on the analysis, the determination of an optimal n_k value for the entire data set will fall between 1 and 3.05. Since the model of Corey [47] predicts the results the closest out of the three models, the optimized n_k value will likely fall near 2 for the entire data set.

5.6. Determining an optimized n_k value

The previous section analyzed the capabilities of selected two-phase pressure models in predicting the experimental results. The homogeneous and relative permeability model of Fourar & Bories [31] predict the data with a mean absolute percent errors of 23.1% and 23.7%, respectively. The separated flow models of Sun & Mishima [40] and English & Kandlikar [38] produce similar mean errors of 23.7% and 22.7%, respectively. By optimizing the relative permeability exponent (n_k) in the two-fluid model, the predictive accuracy can improve.

Fig. 16a shows a comparison of the optimized $n_k = 2.14$ to the experimental measurements. The optimization minimizes the variance between the entire experimental data set and the prediction. The optimized value produces similar statistics (Table 9) to the statistics of Corey [47] shown in Table 8. The similarity of the results indicate the assessment of the data requires further refinement.

Table 9
Overall error statistics for the optimized n_k values in the mixed-wettability experiment.

	$\bar{e}$ (Pa)	σ_e (Pa)	$\bar{e}_{\%}$	$\sigma_{\%}$	$\lvert\bar{e}_{\%}\rvert$
$n_k = 2.14$ (all data)	58.8	462.5	−1.8%	30.4%	25.68%
$n_k = 2.25$ (Entrained-stratified)	86.2	345	8.1%	39.4%	31.5%
$n_k = 3.387$ (Elongated droplet)	−26.9	149	−3.7%	20.7%	16.5%
$n_k = 1.747$ (Rivulet)	−148.6	330.7	−8.42%	17.7%	14.9%
Combined	−93	321	−5.07%	23%	17.8%

As illustrated in Fig. 6, the flow in this work takes on variable patterns: elongated droplet with residual water at low pairs of superficial velocities, entrained stratified flow for low superficial gas velocities with the two highest superficial liquid velocities, and the remaining test conditions produce rivulet type flows. Lewis & Wang [11] and Cho & Wang [45] demonstrated that the n_k value should depend on the flow pattern to account for the changing influence of the liquid on the gas. For $U_L = 5.0 \times 10^{-5}$ m/s the rivulet flow begins at $U_G = 2.54$ m/s, while rivulet flow begins at $U_G = 1.69$ m/s for the three remaining U_L data sets.

The optimization of the n_k value produces varying results depending on the flow regime. The stratified flow with entrained bubbles occurs at $U_L = 1.0 \times 10^{-3}$ and $U_L = 1.0 \times 10^{-2}$ m/s. The optimization produces an $n_k = 2.25$ with a mean absolute percent error of 31.5% (Table 9). The relation under-predicts the experimental data for $U_L = 1.0 \times 10^{-3}$ m/s with a mean absolute percent error of 34% and over-predicts the pressure measurements for $U_L = 1.0 \times 10^{-2}$ m/s with a mean absolute percent error of 30%, which results in the poor agreement of the prediction (Fig. 16b). The optimization indicates that, although visually similar (Fig. 6g and j) the water does not have the same influence in both cases. Additionally, the case of $U_L = 1.0 \times 10^{-3}$ m/s did not correlate well with the elongated droplet flows.

The elongated droplet flow has an optimized n_k value of 3.387 and occurs for the two lowest superficial liquid velocities. The resulting relation under-predicts the $U_L = 5.0 \times 10^{-5}$ m/s data set with a mean error of -116 Pa while over-predicting the $U_L = 5.0 \times 10^{-4}$ m/s data with a mean error of 106 Pa. This results in a mean absolute percent error of 16.5% (Table 9).

The correlation of the remaining data, which corresponds to rivulet type flows, produces an optimized n_k value of 1.747. The n_k value of 1.747 leads to mean errors of $-409, -382, -215$, and 167 Pa for $U_L = 5.0 \times 10^{-5}$ to 1.0×10^{-2} m/s. Thus the optimization under-predicts the three lowest superficial velocities while over-predicting the highest U_L (Fig. 16d). Overall, the mean absolute percent error equals 15% (Table 9).

To accurately compare the optimization to the other models requires combining the error statistics of the three optimized n_k values. Table 9 shows the combination, which results in a mean absolute percent error of 18% and a $\sigma_{\%} = 23\%$. Therefore, the optimization results in a better prediction than the other selected models. However, the optimized n_k values come from the experimental measurements of this work alone, requiring other researchers to add additional measurements in the specific flow regimes to determine the universality of the optimized relative permeability exponents.

5.7. Discussion of the predictive accuracy of the selected models

In the comparison between the experimental data and existing two-phase pressure models, the prediction equations do not collapse the experimental data, leading to the relatively high mean absolute percent errors. Furthermore, determining new correlation parameters (relative permeability exponents, n_k, in the two-fluid model) also fails to collapse the experimental data. As noted in Section 5.2, water entered the downstream pressure tap resulting in an increase in the measured two-phase pressure. Employing an ad hoc method of correcting the two-phase pressure measurements and repeating the analysis shows $\sigma_{\%}$ and $|\bar{e}_{\%}|$ decrease by 3–4% in most cases—particulary increasing for the models that over-predict the $U_L = 1.0 \times 10^{-2}$ m/s data. The method reduces the two-phase pressure by the percentage increase in the single-phase pressure. The difference between the single-phase measurements before and after the experiment, divided by the initial single-phase pressure determines the percent difference. As the two-phase pressure will always have a greater magnitude than the single-phase pressure, this method will produce the greatest reduction of the two-phase pressure. Overall, the change does not produce an appreciable change in the variability of the data.

The experimental design could also play a role in the variability of the data. Water injection occurs 10 mm downstream of the first pressure tap (Fig. 2a). Consequently, the two-phase pressure measurements include the pressure resulting from 10 mm of single-phase flow and any pressure changes associated with the development of the two-phase flow. Section 5.1 noted minimal influence of the development of the single-phase flow on the single-phase measurements relative to fully-developed flow. The analysis using the two-fluid model (Section 5.6) accounts for fully-developed single-phase flow in the 10 mm length via $\bar{z}^*$ in Eq. (12); the variability of the experimental results about the prediction remain. The impact of the two-phase flow development remains a question. In single-phase flows, the development length changes with superficial velocity resulting in different pressures [cf. 54]. Therefore, two-phase flows could also have variable development lengths that would lead to different levels of flow interaction. In the two-fluid model, the n_k value indicates the influence of the interaction between the two-phases. Optimizing the n_k value for each U_L data set gives n_k values of 3.09, 2.60, 2.22, and 1.63 for $U_L = 5.0 \times 10^{-5}$ to 1.0×10^{-2} m/s. The optimization produces mean absolute percent errors of 6.6%, 10.5%, 10.6% and 5.2%, respectively. The range of n_k values indicates the interactions between the phases changes between the data sets. Attempts to experimentally address how the pressure tap location impacts the results by placing a pressure tap after the water injection location produces inconsistent results. Part of the inconsistency results from water entering both pressure taps. Therefore, the experimental design could impact the results but quantitatively how remains unclear.

While experimental limitations will always apply, instabilities of the rivulet could also cause the inability of the two-phase pressure models to collapse the experimental data. In this work, the channel has a base contact angle of 99°. Based on the analysis of Davis [23], Koplik et al. [24], and Herrada et al. [25], this contact angle can result in an unstable rivulet. The rivulet breaking into droplets under multiple test conditions indicates an instability. The syringe pump introduces a characteristic frequency to the system as a result of the steps of the stepper motor. The bubble humidifier also introduces characteristic frequencies based on the frequency of bubble formation. These two mechanisms can provide perturbations to the system that can destabilize the rivulet.

The four superficial liquid velocities produce different Reynolds and Weber numbers, which could lead to different levels of instability between the four data sets based on the analysis of Herrada et al. [25]. In turn, the instability will induce differing levels of interaction between the gas and liquid. Specifically Fig. 6 shows the length of the rivulet before breaking into droplets, the number, and the size of the droplets change between experiments. The selected models do not have a mechanism to account for a rivulet instability and thus the presence of an instability could result in the inability of the models to collapse the data. While rivulet stability remains an open area of research, further conclusions and investigations of the instability in this experiment would require more advanced imaging techniques such as Laser-induced Fluorescence (LIF) and/or schlieren combined with high speed photography to resolve the surface waves/droplet spacing. Particularly, the assessment of the stability condition of Davis [23] would require topological information of the rivulet.

6. Conclusion

This work conducted an experimental study of air-water two-phase frictional pressure drop in a mixed-wettability microchannel of dimensions 3.23 mm wide by 0.304 mm high by 164 mm long. The test conditions produced liquid Reynolds numbers between 0.0277 and 5.55 with a corresponding gas Reynolds number ranging between 18.2 and 197. Compared to the measured two-phase pressure drop in a hydrophilic microchannel of the same dimensions but differing only in the base contact angle, the two-phase pressure drop increased when the base contact angle changed from 76° to 99°. The flow in the mixed-wettability channel formed primarily as rivulet type flow compared to the stratified flow in the hydrophilic channel. The flow behavior varied between experiments for fixed test conditions, resulting in different two-phase pressure drops.

Researchers have found inconsistent trends in how the two-phase pressure drop changes when comparing hydrophobic to hydrophilic microchannels. Based on the current study and the selected works, consistency results from classifying adiabatic two-phase flow experiments in a single microchannel into three categories: homogeneous, hydrophobic mixed-wettability, and superhydrophobic mixed-wettability microchannels. For the discussed hydrophobic mixed-wettability microchannels and the current work, the two-phase pressure increases relative to a hydrophilic microchannel. For the two superhydrophobic mixed-wettability channels analyzed the opposite occurs, the two-phase pressure will decrease relative to a hydrophilic microchannel. In both cases, the behavior did not depend on the liquid-only Reynolds number, liquid Capillary number, nor scale. The selected homogeneous microchannel experiments became consistent with hydraulic diameter only.

Comparing the two-phase pressure drop predicted by several models showed the correlations for the separated flow model proposed by Sun & Mishima [40] and English & Kandlikar [38] predicted the experimental two-phase pressure with mean absolute percent errors of 23.7% and 22.7%, respectively. Optimizing the relative permeability exponent (n_k) for each of the three flow patterns improved the prediction to a mean absolute percent error of 17.8%. An optimized n_k value for rivulet flows alone equals 1.747 and predicted the two-phase pressure drop of rivulet flows with a mean absolute percent error of 14.9%. The selected models, including the optimization of the two-fluid model, did not collapse the experimental two-phase pressure. Analysis using the two-fluid model indicates differing levels of interaction between the air and water for different test cases. This differing interaction could result from the inclusion of the two-phase flow development region in the measurements and/or an instability of the rivulet—for which the test conditions favor—leading to the inability of the models to collapse the experimental data.

Acknowledgements

The authors gratefully acknowledge UCI's machinist, Tucker Parris, for his guidance in machining the PTFE base. In addition, the authors thank Professor John C. LaRue for his advice. Y. Wang thanks the Shanghai Everpower Technologies Ltd. for their partial financial support in PEM fuel cell research.

References

[1] C. Fang, J.E. Steinbrenner, F.M. Wang, K.E. Goodson, Impact of wall hydrophobicity on condensation flow and heat transfer in silicon microchannels, J. Micromech. Microeng. 20 (4) (2010) 045018, https://doi.org/10.1088/0960-1317/20/4/045018.

[2] C. Choi, J.S. Shin, D.I. Yu, M.H. Kim, Flow boiling behaviors in hydrophilic and hydrophobic microchannels, Exp. Thermal Fluid Sci. 35 (5) (2011) 816–824, https://doi.org/10.1016/j.expthermflusci.2010.07.003.

[3] H. Jo, H.S. Ahn, S. Kang, M.H. Kim, A study of nucleate boiling heat transfer on hydrophilic, hydrophobic and heterogeneous wetting surfaces, Int. J. Heat Mass Transf. 54 (25) (2011) 5643–5652, https://doi.org/10.1016/j.ijheatmasstransfer.2011.06.001.

[4] S. Park, B.N. Popov, Effect of cathode GDL characteristics on mass transport in PEM fuel cells, Fuel 88 (11) (2009) 2068–2073, https://doi.org/10.1016/j.fuel.2009.06.020.

[5] Y. Wang, K.S. Chen, J. Mishler, S.C. Cho, X.C. Adroher, A review of polymer electrolyte membrane fuel cells: technology, applications, and needs on fundamental research, Appl. Energy 88 (4) (2011) 981–1007, https://doi.org/10.1016/j.apenergy.2010.09.030.

[6] J. Owejan, T. Trabold, D. Jacobson, M. Arif, S. Kandlikar, Effects of flow field and diffusion layer properties on water accumulation in a PEM fuel cell, Int. J. Hydrogen Energy 32 (17) (2007) 4489–4502, https://doi.org/10.1016/j.ijhydene.2007.05.044.

[7] Y. Cai, J. Hu, H. Ma, B. Yi, H. Zhang, Effects of hydrophilic/hydrophobic properties on the water behavior in the micro-channels of a proton exchange membrane fuel cell, J. Power Sources 161 (2) (2006) 843–848, https://doi.org/10.1016/j.jpowsour.2006.04.110.

[8] Z. Lu, C. Rath, G. Zhang, S.G. Kandlikar, Water management studies in PEM fuel cells, part IV: Effects of channel surface wettability, geometry and orientation on the two-phase flow in parallel gas channels, Int. J. Hydrogen Energy 36 (16) (2011) 9864–9875, https://doi.org/10.1016/j.ijhydene.2011.04.226.

[9] C.Y. Lee, S.Y. Lee, Pressure drop of two-phase plug flow in round mini-channels: influence of surface wettability, Exp. Thermal Fluid Sci. 32 (8) (2008) 1716–1722, https://doi.org/10.1016/j.expthermflusci.2008.06.007.

[10] X. Wang, Y. Yong, C. Yang, Z.S. Mao, D. Li, Investigation on pressure drop characteristic and mass transfer performance of gas-liquid flow in micro-channels, Microfluid. Nanofluid. 16 (1) (2014) 413–423, https://doi.org/10.1007/s10404-013-1226-5.

[11] J.M. Lewis, Y. Wang, Two-phase frictional pressure drop and water film thickness in a thin hydrophilic microchannel, Int J. Heat Mass Transf. 127 (2018) 813–828, https://doi.org/10.1016/j.ijheatmasstransfer.2018.08.060.

[12] K.A. Stevens, J. Crockett, D.R. Maynes, B.D. Iverson, Two-phase flow pressure drop in superhydrophobic channels, Int. J. Heat Mass Transf. 110 (2017) 515–522, https://doi.org/10.1016/j.ijheatmasstransfer.2017.03.055.

[13] S.M. Kim, I. Mudawar, Universal approach to predicting two-phase frictional pressure drop for adiabatic and condensing mini/micro-channel flows, Int. J. Heat Mass Transf. 55 (11) (2012) 3246–3261, https://doi.org/10.1016/j.ijheatmasstransfer.2012.02.047.

[14] Y. Wang, S. Al Shakhshir, X. Li, P. Chen, Superhydrophobic flow channel surface and its impact on pem fuel cell performance, Int. J. Low-Carbon Technol. 9 (3) (2014) 225–236, https://doi.org/10.1093/ijlct/cts069.

[15] S.C. Cho, Y. Wang, Two-phase flow dynamics in a micro channel with heterogeneous surfaces, Int. J. Heat Mass Transf. 71 (2014) 349–360, https://doi.org/10.1016/j.ijheatmasstransfer.2013.12.023.

[16] H.T. Phan, N. Caney, P. Marty, S. Colasson, J. Gavillet, Flow boiling of water in a minichannel: the effects of surface wettability on two-phase pressure drop, Appl. Therm. Eng. 31 (11) (2011) 1894–1905, https://doi.org/10.1016/j.applthermaleng.2011.02.036.

[17] C. Choi, D.I. Yu, M. Kim, Surface wettability effect on flow pattern and pressure drop in adiabatic two-phase flows in rectangular microchannels with t-junction mixer, Exp. Thermal Fluid Sci. 35 (6) (2011) 1086–1096, https://doi.org/10.1016/j.expthermflusci.2011.03.003.

[18] P. Rapolu, S.Y. Son, Characterization of wettability effects on pressure drop of two-phase flow in microchannel, Exp. Fluids 51 (4) (2011) 1101–1108, https://doi.org/10.1007/s00348-011-1129-8.

[19] A. Barajas, R. Panton, The effects of contact angle on two-phase flow in capillary tubes, Int. J. Multiph. Flow 19 (2) (1993) 337–346, https://doi.org/10.1016/0301-9322(93)90007-H.

[20] C.Y. Lee, S.Y. Lee, Influence of surface wettability on transition of two-phase flow pattern in round mini-channels, Int. J. Multiph. Flow 34 (7) (2008) 706–711, https://doi.org/10.1016/j.ijmultiphaseflow.2008.01.002.

[21] D. Huh, C.H. Kuo, J.B. Grotberg, S. Takayama, Gasliquid two-phase flow patterns in rectangular polymeric microchannels: effect of surface wetting properties, New J. Phys. 11 (7) (2009) 075034.

[22] J.A. Diez, A.G. Gonzlez, L. Kondic, On the breakup of fluid rivulets, Phys. Fluids 21 (8) (2009) 082105, https://doi.org/10.1063/1.3211248.

[23] S.H. Davis, Moving contact lines and rivulet instabilities. Part 1. the static rivulet, J. Fluid Mech. 98 (2) (1980) 225–242, https://doi.org/10.1017/S0022112080000110.

[24] J. Koplik, T.S. Lo, M. Rauscher, S. Dietrich, Pearling instability of nanoscale fluid flow confined to a chemical channel, Phys. Fluids 18 (3) (2006) 032104, https://doi.org/10.1063/1.2178786.

[25] M.A. Herrada, A. Mohamed, J.M. Montanero, A. Gan-Calvo, Stability of a rivulet flowing in a microchannel, Int. J. Multiph. Flow 69 (2015) 1–7, https://doi.org/10.1016/j.ijmultiphaseflow.2014.10.012.

[26] V.V. Cheverda, A. Glushchuk, P. Queeckers, S.B. Chikov, O.A. Kabov, Liquid rivulets moved by shear stress of gas flow at altered levels of gravity, Microgravity Sci. Technol. 25 (1) (2013) 73–81, https://doi.org/10.1007/s12217-012-9335-4.

[27] W. McAdams, W. Woods, I. Heroman Jr., Vaporization inside horizontal tubes—II benzene-oil mixtures, Trans. ASME 64 (1) (1942) 193–200.

[28] A. Cicchitti, C. Lombardi, M. Silvestri, G. Soldaini, R. Zavattarelli, Two-phase cooling experiments: pressure drop, heat transfer and burnout measurements, Energia Nucleare 7 (6) (1960) 407–425.

[29] S. Lin, C. Kwok, R.Y. Li, Z.H. Chen, Z.Y. Chen, Local frictional pressure drop during vaporization of r-12 through capillary tubes, Int. J. Multiph. Flow 17 (1) (1991) 95–102, https://doi.org/10.1016/0301-9322(91)90072-B.

[30] A. Dukler, M. Wicks III, R. Cleveland, Frictional pressure drop in two-phase flow: B. an approach through similarity analysis, AIChE J. 10 (1) (1964) 44–51, https://doi.org/10.1002/aic.690100118.

[31] M. Fourar, S. Bories, Experimental study of air-water two-phase flow through a fracture (narrow channel), Int. J. Multiph. Flow 21 (4) (1995) 621–637, https://doi.org/10.1016/0301-9322(95)00005-I.

[32] D. Beattie, P. Whalley, A simple two-phase frictional pressure drop calculation method, Int. J. Multiph. Flow 8 (1) (1982) 83–87, https://doi.org/10.1016/0301-9322(82)90009-X.

[33] M. Awad, Y. Muzychka, Effective property models for homogeneous two-phase flows, Exp. Thermal Fluid Sci. 33 (1) (2008) 106–113, https://doi.org/10.1016/j.expthermflusci.2008.07.006.

[34] R. Lockhart, R. Martinelli, Proposed correlation of data for isothermal two-phase, two-component flow in pipes, Chem. Eng. Prog. 45 (1949) 39–48.

[35] D. Chisholm, A theoretical basis for the Lockhart-Martinelli correlation for two-phase flow, Int. J. Heat Mass Transf. 10 (12) (1967) 1767–1778, https://doi.org/10.1016/0017-9310(67)90047-6.

[36] K. Mishima, T. Hibiki, Some characteristics of air-water two-phase flow in small diameter vertical tubes, Int. J. Multiph. Flow 22 (4) (1996) 703–712, https://doi.org/10.1016/0301-9322(96)00010-9.

[37] W. Zhang, T. Hibiki, K. Mishima, Correlations of two-phase frictional pressure drop and void fraction in mini-channel, Int. J. Heat Mass Transf. 53 (1) (2010) 453–465, https://doi.org/10.1016/j.ijheatmasstransfer.2009.09.011.

[38] N.J. English, S.G. Kandlikar, An experimental investigation into the effect of surfactants on air-water two-phase flow in minichannels, Heat Transfer Eng. 27 (4) (2006) 99–109, https://doi.org/10.1080/01457630500523980.

[39] W. Li, Z. Wu, A general correlation for adiabatic two-phase pressure drop in micro/mini-channels, Int. J. Heat Mass Transf. 53 (13) (2010) 2732–2739, https://doi.org/10.1016/j.ijheatmasstransfer.2010.02.029.

[40] L. Sun, K. Mishima, Evaluation analysis of prediction methods for two-phase flow pressure drop in mini-channels, Int. J. Multiph. Flow 35 (1) (2009) 47–54, https://doi.org/10.1016/j.ijmultiphaseflow.2008.08.003.

[41] Y. Ma, X. Ji, D. Wang, T. Fu, C. Zhu, Measurement and correlation of pressure drop for gas-liquid two-phase flow in rectangular microchannels, Chin. J. Chem. Eng. 18 (6) (2010) 940–947, https://doi.org/10.1016/S1004-9541(09)60151-8.

[42] X. Li, T. Hibiki, Frictional pressure drop correlation for two-phase flows in mini and micro single-channels, Int. J. Multiph. Flow 90 (Supplement C) (2017) 29–45, https://doi.org/10.1016/j.ijmultiphaseflow.2016.12.003.

[43] H.J. Lee, S.Y. Lee, Pressure drop correlations for two-phase flow within horizontal rectangular channels with small heights, Int. J. Multiph. Flow 27 (5) (2001) 783–796, https://doi.org/10.1016/S0301-9322(00)00050-1.

[44] S. Saisorn, S. Wongwises, The effects of channel diameter on flow pattern, void fraction and pressure drop of two-phase airwater flow in circular micro-channels, Exp. Thermal Fluid Sci. 34 (4) (2010) 454–462, https://doi.org/10.1016/j.expthermflusci.2009.02.006.

[45] S.C. Cho, Y. Wang, Two-phase flow dynamics in a micro hydrophilic channel: a theoretical and experimental study, Int. J. Hear Mass Transfer 70 (12) (2014) 340–352, https://doi.org/10.1016/j.ijheatmasstransfer.2013.11.003.

[46] Y. Wang, Porous-media flow fields for polymer electrolyte fuel cells II. Analysis of channel two-phase flow, J. Electrochem. Soc. 156 (2009) B1134–B1141, https://doi.org/10.1149/1.3183785.

[47] A. Corey, The interrelation between gas and oil relative permeabilities, Producers Mon. 19 (1954) 38–41.

[48] A. Nowamooz, G. Radilla, M. Fourar, Non-Darcian two-phase flow in a transparent replica of a rough-walled rock fracture, Water Resour. Res. 45 (7) (2009) 1–9, https://doi.org/10.1029/2008WR007315.

[49] C.Y. Chen, R.N. Horne, M. Fourar, Experimental study of liquid-gas flow structure effects on relative permeabilities in a fracture, Water Resour. Res. 40 (8) (2004) 1–15, https://doi.org/10.1029/2004WR003026.

[50] Fourar M, Lenormand R. A viscous coupling model for relative permeabilities in a fracture. SPE Annual Technical Conference and Exhibition, September 27–30; Society of Petroleum Engineers; 1998: doi: 10.2118/49006-MS.

[51] H. Huang, Z. Li, S. Liu, Xy Lu, Shan-and-chen-type multiphase lattice boltzmann study of viscous coupling effects for two-phase flow in porous media, Int. J. Numer. Meth. Fluids 61 (3) (2009) 341–354, https://doi.org/10.1002/fld.1972.

[52] S. Kakac, R. Shah, W. Aung, Handbook of Single-Phase Convective Heat Transfer, Wiley, 1987.

[53] Shah R, London A. Laminar Flow Forced Convection Heat Transfer and Flow Friction in Straight and Curved Ducts–A Summary of Analytical Solutions. Tech. Rep.; Standford University. Department of Mechanical Engineering; 1971.

[54] R. Shah, A correlation for laminar hydrodynamic entry length solutions for circular and noncircular ducts, J. Fluids Eng. 100 (1978) 177–179, https://doi.org/10.1115/1.3448626.

[55] B.M. Jose, T. Cubaud, Formation and dynamics of partially wetting droplets in square microchannels, RSC Adv. 4 (2014) 14962–14970, https://doi.org/10.1039/C4RA00654B.

[56] G. Flipo, C. Josset, J. Bellettre, B. Auvity, Clarification of the surface wettability effects on two-phase flow patterns in PEMFC gas channels, Int. J. Hydrogen Energy 41 (34) (2016) 15518–15527, https://doi.org/10.1016/j.ijhydene.2016.04.008.

[57] J.P. Rothstein, Slip on superhydrophobic surfaces, Annu. Rev. Fluid Mech. 42 (1) (2010) 89–109, https://doi.org/10.1146/annurev-fluid-121108-145558.

[58] C. Lee, C.H. Choi, C.J. Kim, Superhydrophobic drag reduction in laminar flows: a critical review, Exp. Fluids 57 (12) (2016) 176, https://doi.org/10.1007/s00348-016-2264-z.